

**AEDC-TR-74-30**

cy. 5

DEC 9 1974  
JAN 3 1975  
SEP 1 1988



**STATIC PRESSURE ON SHARP AND BLUNT CONES IN  
CONICAL AND PARALLEL LOW-DENSITY FLOW**

**Max Kinslow  
ARO, Inc.**

**VON KÁRMÁN GAS DYNAMICS FACILITY  
ARNOLD ENGINEERING DEVELOPMENT CENTER  
AIR FORCE SYSTEMS COMMAND  
ARNOLD AIR FORCE STATION, TENNESSEE 37389**

**November 1974**

**Final Report for Period October 1, 1971 – March 31, 1972**

Approved for public release; distribution unlimited.

**Prepared for**

**ARNOLD ENGINEERING DEVELOPMENT CENTER (DY)  
ARNOLD AIR FORCE STATION, TENNESSEE 37389**

## NOTICES

When U. S. Government drawings specifications, or other data are used for any purpose other than a definitely related Government procurement operation, the Government thereby incurs no responsibility nor any obligation whatsoever, and the fact that the Government may have formulated, furnished, or in any way supplied the said drawings, specifications, or other data, is not to be regarded by implication or otherwise, or in any manner licensing the holder or any other person or corporation, or conveying any rights or permission to manufacture, use, or sell any patented invention that may in any way be related thereto.

Qualified users may obtain copies of this report from the Defense Documentation Center.

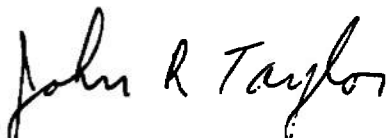
References to named commercial products in this report are not to be considered in any sense as an endorsement of the product by the United States Air Force or the Government.

This report has been reviewed by the Information Office (OI) and is releasable to the National Technical Information Service (NTIS). At NTIS, it will be available to the general public, including foreign nations.

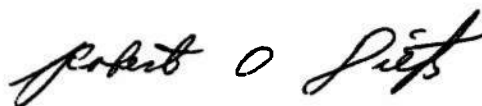
## APPROVAL STATEMENT

This technical report has been reviewed and is approved for publication.

FOR THE COMMANDER



JOHN R. TAYLOR  
Lt Colonel, USAF  
Chief, Research and  
Development Division



ROBERT O. DIETZ  
Director of Technology

# UNCLASSIFIED

REPORT DOCUMENTATION PAGE		READ INSTRUCTIONS BEFORE COMPLETING FORM
1. REPORT NUMBER <b>AEDC-TR-74-30</b>	2. GOVT ACCESSION NO.	3. RECIPIENT'S CATALOG NUMBER
4. TITLE (and Subtitle) <b>STATIC PRESSURE ON SHARP AND BLUNT CONES IN CONICAL AND PARALLEL LOW-DENSITY FLOW</b>		5. TYPE OF REPORT & PERIOD COVERED <b>Final Report - October 1, 1971-March 31, 1972</b>
		6. PERFORMING ORG. REPORT NUMBER
7. AUTHOR(s) <b>Max Kinslow, ARO, Inc.</b>		8. CONTRACT OR GRANT NUMBER(s)
9. PERFORMING ORGANIZATION NAME AND ADDRESS <b>Arnold Engineering Development Center Arnold Air Force Station, Tennessee 37389</b>		10. PROGRAM ELEMENT, PROJECT, TASK AREA & WORK UNIT NUMBERS <b>Program Element 65802F</b>
11. CONTROLLING OFFICE NAME AND ADDRESS <b>Arnold Engineering Development Center (DYFS) Arnold Air Force Station, Tennessee 37389</b>		12. REPORT DATE <b>November 1974</b>
		13. NUMBER OF PAGES <b>72</b>
14. MONITORING AGENCY NAME & ADDRESS (if different from Controlling Office)		15. SECURITY CLASS. (of this report)  <b>UNCLASSIFIED</b>
		15a. DECLASSIFICATION/DOWNGRADING SCHEDULE <b>N/A</b>
16. DISTRIBUTION STATEMENT (of this Report) <b>Approved for public release; distribution unlimited.</b>		
17. DISTRIBUTION STATEMENT (of the abstract entered in Block 20, if different from Report)		
18. SUPPLEMENTARY NOTES  <b>Available in DDC.</b>		
19. KEY WORDS (Continue on reverse side if necessary and identify by block number)		
<b>static pressure</b> <b>cones</b> <b>rarefied gas dynamics</b> <b>pressure distribution</b>	<b>nozzles</b> <b>orifices</b> <b>Mach number</b> <b>Reynolds number</b>	<b>wind tunnel test</b> <b>environmental</b> <b>simulation</b>
20. ABSTRACT (Continue on reverse side if necessary and identify by block number)		
<p>The static pressure distribution on sharp and blunt 10-deg half-angle cones was measured under rarefied conditions in both a uniform and a source flow field. Angle of attack of the cones was varied up to 10 deg. Pressure distributions are presented for cold-wall conditions at <math>18.0 \leq M_\infty \leq 20.3</math> and <math>407 &lt; Re_\infty/in. \leq 1272</math>. The source flow results are corrected according to the Newtonian</p>		

# UNCLASSIFIED

# UNCLASSIFIED

20. Continued.

pressure distribution, and the results agree with the uniform flow measurements for the longitudinal distribution at zero angle of attack. Comparisons are made with previous experimental and theoretical results.

# UNCLASSIFIED

## PREFACE

The research reported herein was conducted at the Arnold Engineering Development Center (AEDC), Air Force Systems Command (AFSC), Arnold Air Force Station, Tennessee. The results presented were obtained by ARO, Inc. (a subsidiary of Sverdrup & Parcel and Associates, Inc.), contract operator of AEDC, AFSC, Arnold Air Force Station, Tennessee. Tests were conducted under Project No. VM2266. The manuscript (ARO Control No. ARO-VKF-TR-74-10) was submitted for publication on January 16, 1974.

## CONTENTS

	<u>Page</u>
1.0 INTRODUCTION . . . . .	7
2.0 APPARATUS	
2.1 Tunnel M. . . . .	7
2.2 Nozzle Flow Conditions . . . . .	9
2.3 Models . . . . .	10
2.4 Tunnel Instrumentation and Data Acquisition System. . . . .	14
3.0 RESULTS AND DISCUSSION	
3.1 Procedure . . . . .	14
3.2 Orifice Correction . . . . .	15
3.3 Pressure Correction for Source Flow Effects . . . . .	17
3.4 Experimental Results . . . . .	24
4.0 SUMMARY AND CONCLUDING REMARKS. . . . .	49
REFERENCES . . . . .	50

## ILLUSTRATIONS

Figure

1. Tunnel M	
a. Photograph . . . . .	8
b. Elevation View . . . . .	8
2. Pitot Pressure Ratio for Contoured and Conical Nozzles . . . . .	11
3. Model Schematic . . . . .	13
4. Body Coordinate System . . . . .	18
5. Plot of Eq. (17) for $l_1/L = 0$ . . . . .	20
6. Plot of Eq. (17) for $l_1/L = 0.2$ . . . . .	21
7. Ratio of Uniform and Source Flow Pressure Coefficient for $l_1/L = 0$ . . . . .	22
8. Ratio of Uniform and Source Flow Pressure Coefficient for $l_1/L = 0.2$ . . . . .	23
9. Normalized Axial Source Flow Effect . . . . .	24
10. Variation of Newtonian Pressure Coefficient Ratio with Angle of Attack . . . . .	25

<u>Figure</u>	<u>Page</u>
11. Sharp Cone Experimental Pressure Coefficient in the Contoured Nozzle for $\phi = 0$ deg, 180 deg . . . . .	26
12. Sharp Cone Experimental Pressure Coefficient in the Contoured Nozzle for $\phi = 90$ deg, 270 deg . . . . .	27
13. Sharp Cone Experimental Pressure Coefficient for Condition I in the Conical Nozzle for $x = 0$ and $\phi = 0$ deg, 180 deg. . . . .	28
14. Sharp Cone Experimental Pressure Coefficient for Condition I in the Conical Nozzle for $x = 0$ and $\phi = 90$ deg, 270 deg . . . . .	29
15. Sharp Cone Experimental Pressure Coefficient for Condition I in the Conical Nozzle for $x = 12$ in. and $\phi = 90$ deg, 270 deg . . . . .	30
16. Sharp Cone Experimental Pressure Coefficient for Condition II in the Conical Nozzle for $x = 0$ and $\phi = 0$ deg, 180 deg. . . . .	31
17. Sharp Cone Experimental Pressure Coefficient for Condition II in the Conical Nozzle for $x = 0$ and $\phi = 90$ deg, 270 deg . . . . .	32
18. Sharp Cone Experimental Pressure Coefficient for Condition II in the Conical Nozzle for $x = 12$ in. and $\phi = 90$ deg, 270 deg . . . . .	33
19. Experimental Variation of Pressure Coefficient Ratio with Angle of Attack for the Sharp Cone in the Contoured Nozzle . . . . .	34
20. Experimental Variation of Pressure Coefficient Ratio with Angle of Attack for the Sharp Cone in the Conical Nozzle . . . . .	35
21. Calculated Inviscid Pressure on 10-deg Sharp Cone . . . . .	36
22. Sharp Cone Surface Pressure Measurements under Uniform and Source Flow Conditions . . . . .	37
23. Sharp Cone Pressure Distribution Corrected for Source Flow Effects . . . . .	38
24. Present Data Uncorrected for Orifice or Source Flow Effects . . . . .	40

<u>Figure</u>	<u>Page</u>
25. Blunt Cone Experimental Pressure Coefficient in the Contoured Nozzle for $\phi = 0, 180$ deg. . . . .	41
26. Blunt Cone Experimental Pressure Coefficient in the Contoured Nozzle for $\phi = 90$ deg, 270 deg . . . . .	42
27. Blunt Cone Experimental Pressure Coefficient for Conditions I in the Conical Nozzle for $x = 0$ and $\phi = 90$ deg, 270 deg . . . . .	43
28. Blunt Cone Experimental Pressure Coefficient for Conditions II in the Conical Nozzle for $x = 0$ and $\phi = 0$ deg, 180 deg. . . . .	44
29. Blunt Cone Experimental Pressure Coefficient for Conditions II in the Conical Nozzle for $x = 0$ and $\phi = 90$ deg, 270 deg . . . . .	45
30. Experimental Variation of Pressure Coefficient Ratio with Angle of Attack for the Blunt Cone . . . . .	46
31. Experimental Blunt Cone Results for $\alpha = 0$ as a Function of Cheng's Parameters . . . . .	47
32. Blunt Cone Pressure Distribution Corrected for Source Flow Effects . . . . .	48
33. Comparison of Present Results with those of Vas . . . . .	49

## TABLES

1. Nominal Flow Conditions . . . . .	12
2. Pressure Orifice Schedule . . . . .	13

## APPENDIXES

A. CORRECTION OF PITOT PRESSURE ORIFICE AND PROBE EFFECTS . . . . .	55
B. REEVALUATION OF PARAMETERS RELATIVE TO THE ORIFICE EFFECT . . . . .	61
NOMENCLATURE . . . . .	70



## 1.0 INTRODUCTION

In the high Reynolds number range of conventional wind tunnels, contoured nozzles are commonly used in order to obtain uniform test conditions. One nozzle can operate over a wide range of pressures and temperatures for a given Mach number. However, this is not the case in the low Reynolds number regime, where the boundary-layer displacement thickness may be comparable to the physical dimensions of the nozzle. In this flow regime a contoured nozzle can produce a uniform, shock-free flow at only one fixed condition. Attempts to extend the operating range by various means have met with little success (see Ref. 1).

Most low-density wind tunnels in the past have utilized conical nozzles, with their resultant flow nonuniformities, to produce the test section conditions. This has limited flow usefulness and model size. For larger and/or slender models it is necessary to correct the experimental results from such nozzles for source flow effects and other flow nonuniformities in order to obtain useful data.

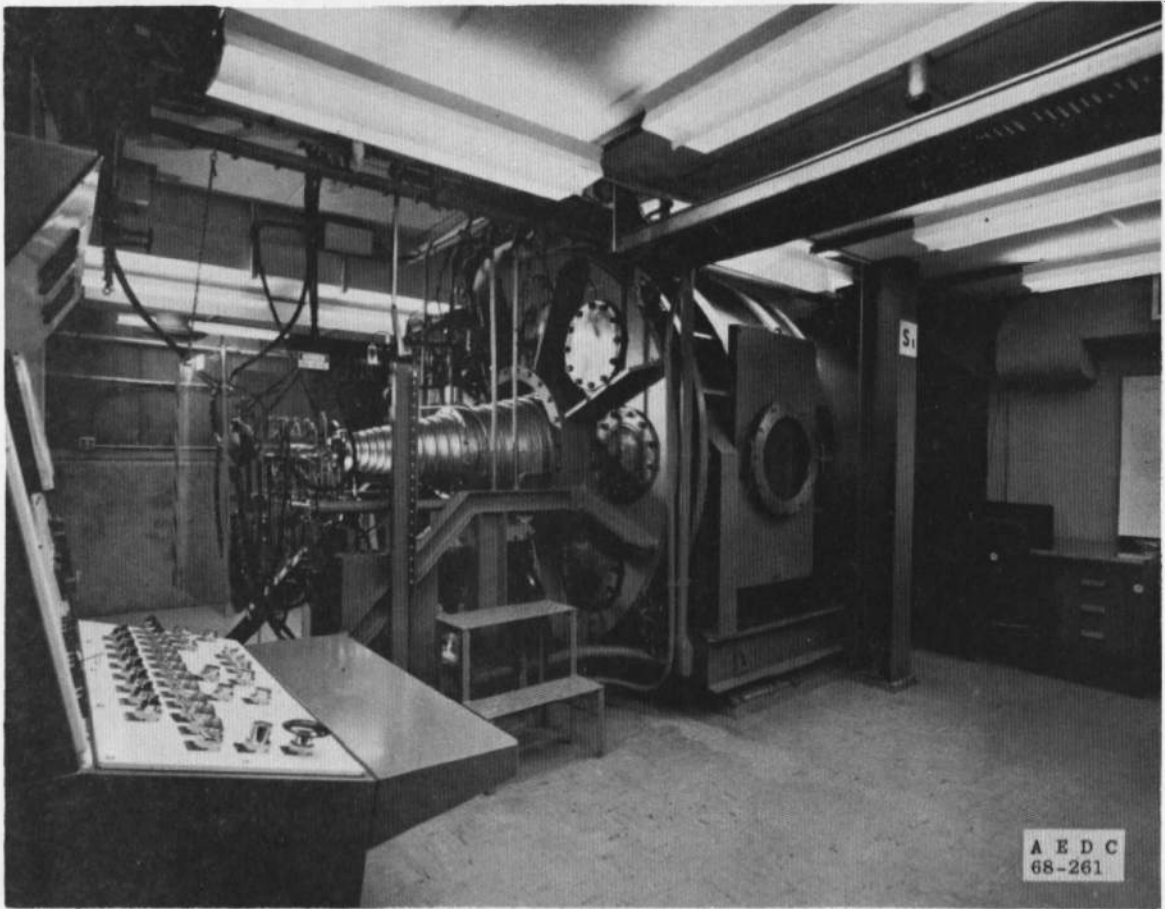
In order to fully compare results from various labs for both contoured and conical nozzles, a cooperative data exchange agreement (DEA) involving Deutsche Forschungs und Versuchsanstalt für Luft-Raumfahrt (DFVLR), the Air Force Flight Dynamics Laboratory (AFFDL), and the Arnold Engineering Development Center (AEDC) was formulated. Agreement was reached on the use of standard 10-deg half-angle blunt and sharp cone models for comparison of results from the various facilities.

The first phase of the AEDC investigation was the measurement of heat transfer and static pressure on standard 10-deg sharp and blunt cones in Tunnel M utilizing both contoured and conical nozzles. The heat-transfer phase of this project was completed first and has been reported by Boylan (Ref. 2).

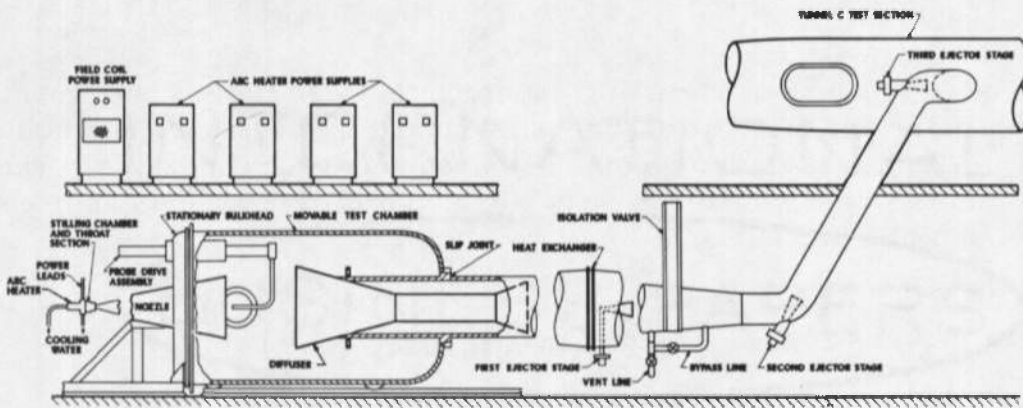
## 2.0 APPARATUS

### 2.1 TUNNEL M

The von Kármán Gas Dynamics Facility (VKF) Tunnel M, shown photographically in Fig. 1a and schematically in Fig. 1b, is a continuous,



a. Photograph



ELEVATION VIEW OF TUNNEL M

b. Elevation view  
Figure 1. Tunnel M.

arc-heated, low-density, hypersonic wind tunnel normally using nitrogen as the test gas. Pumping is provided by three stages of air ejectors in series which exhaust into the VKF main compressor system through the AEDC-VKF Tunnel C test section. This arrangement permits simultaneous operation of these two tunnels, or either can be operated alone. Tunnel M consists basically of the following major components, in streamwise order:

1. Rotating-arc, d-c arc heater of AEDC-VKF design with a power supply rated at 200 kw for continuous operation. Gas is injected into the arc heater tangentially.
2. Cylindrical settling chamber of 3.8-cm (1.5-in.) diameter and 7.6-cm (3.0-in.) length.
3. Both an axisymmetric, contoured, Mach 18 nozzle and a 14-deg, half-angle, conical nozzle were used in the present study.
4. Stationary bulkhead of 2.4-m (8-ft) diameter, which supports the nozzle, probe drive, and model support system. The bulkhead contains eight 30-cm (12-in.)-diam ports.
5. Cylindrical 2.4-m (8-ft)-diam test chamber which moves downstream to allow access to the test section, models, and probes.
6. Axisymmetric diffuser with convergent entrance, constant area throat, and divergent outlet. Interchangeable units are available for different test configurations.
7. Downstream heat exchanger.
8. First air ejector stage.
9. Isolation valve.
10. Second and third air ejector stages.
11. Connection of the AEDC-VKF Tunnel C test section.

The arc heater, settling chamber, and nozzle are backside water cooled.

## 2.2 NOZZLE FLOW CONDITIONS

Nozzle test section conditions are determined by a measurement of test section pitot pressure,  $p'_0$ , stilling chamber total pressure,  $p_0$ , and

the total nozzle mass flow rate,  $\dot{m}$ . By knowing the nozzle throat area,  $A^*$ , and the discharge coefficient, which are determined by independent measurement, together with  $p_0$  and  $\dot{m}$ , the stagnation temperature,  $T_0$ , can be calculated. The basic assumption of the flow calibration is that thermodynamic equilibrium exists in the stilling chamber and the vibrational mode of the nitrogen becomes frozen at the nozzle sonic point. The gas is assumed to behave as a perfect gas downstream of the nozzle throat. Previous measurements using calorimeters, electron beam techniques, and mass flux probes have confirmed the validity of this flow calibration procedure for Tunnel M. The method of determining  $T_0$  is given in Ref. 3.

The measured test section pitot pressure under rarefied conditions is not equal to the stagnation pressure downstream of a normal shock as is usually assumed, but must be corrected for both probe and orifice effects. The correction scheme used to obtain the true pitot pressure is given in Appendix A.

Both the Mach 18 contoured nozzle and the 14-deg, half-angle conical nozzle were utilized for the present test. The conical nozzle was operated at two different flow conditions with the model tested at the nozzle exit and at a point 12 in. downstream of the exit. Since an axial gradient existed in the conical nozzle, this produced four distinct test conditions in that nozzle. This, together with the contoured nozzle conditions, gave a total of five test conditions.

Figure 2 shows the ratio,  $p'_0/p_0$ , as a function of axial distance from the nozzle exit,  $x$ , for the two nozzles. The pitot pressure,  $p'_0$ , has been corrected by the method given in Appendix A. Table 1 gives the nominal test conditions for the five flow conditions. Also given is the approximate usable test section diameter. For a given test condition the flow parameters varied slightly from run to run. In order to account for this variation, an impact probe was mounted on the probe drive unit so that it could be moved into the test section near the model nose any time it was desirable to check flow conditions. All other quantities were measured simultaneously with model pressures.

## 2.3 MODEL

The model tested was a 10-deg, half-angle cone with interchangeable noses. Two different noses were tested. One was a blunt nose with a radius,  $R_n$ , of 0.9 cm (0.354 in.) and the other a sharp nose,

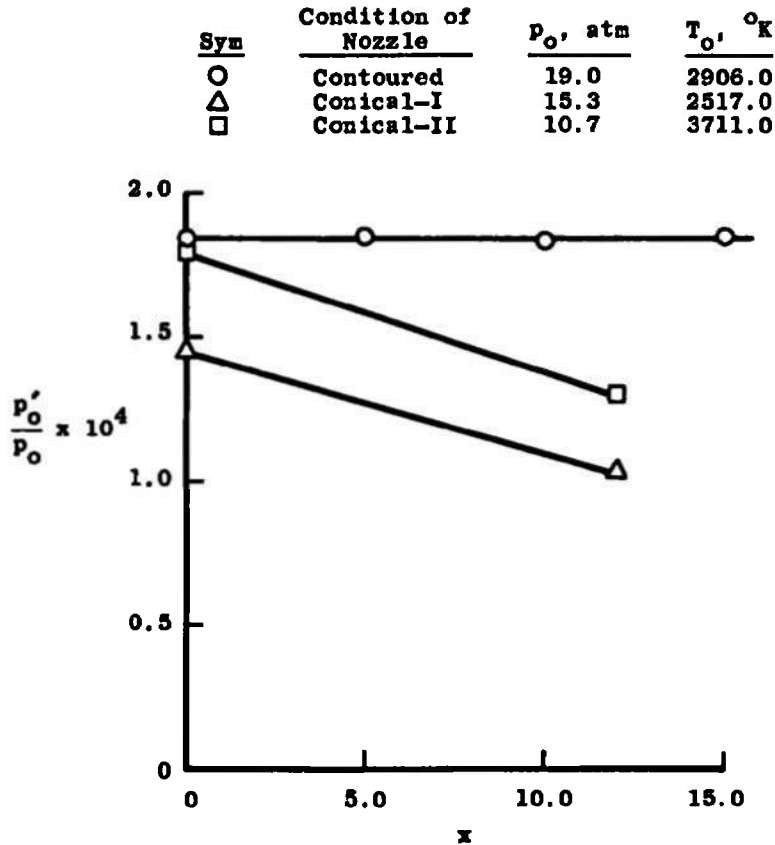


Figure 2. Pitot pressure ratio for contoured and conical nozzles.

$R_n \approx 0.00025$  cm (0.001 in.). The model was one of the same models used for the heat-transfer phase of this project (see Ref. 2). The heat-transfer gages were removed and replaced by static pressure tubes for the present test. Because of restricted internal space, it was not possible to install pressure tubes at all locations.

The body of the model was cooled by means of water-cooling tubes soldered to the inside surface of the model. The interchangeable noses were uncooled except by means of radiation and conduction to the water-cooled portion of the model. A schematic of the model is shown in Fig. 3. The model contained five pressure sensing orifices, one of which is located 180 deg away from the others, so as to check model alignment and flow angularity. The pressure orifice diameter was 0.322 cm (0.127 in.). The schedule of orifice location for both model configurations is given in Table 2.

**Table 1. Nominal Flow Conditions**  
**a. Customary Units**

Nozzle	Contoured		Conical-Condition 1		Conical-Condition II	
	Nozzle Exit	Nozzle Exit	12-in. Outside Exit	Nozzle Exit	12-in. Outside Exit	
$P_0$ , atm	19.00	15.28	15.31	10.72	10.76	
$T_0$ , °K	2900	2517	2552	3711	3703	
$h_0$ , Btu/lbm	1505	1284	1304	1966	1961	
$M_0$	18.01	18.91	20.29	18.14	19.32	
$Re_0$ , in. <sup>-1</sup>	1272	1100	877	486	407	
$P_w$ , μHg	6.38	3.66	2.26	3.43	2.23	
$T_w$ , °K	46.07	36.23	31.96	58.18	51.28	
$U_w$ , ft/sec	8180	7613	7674	9258	9256	
$\rho_w$ , lbm/ft <sup>3</sup>	$3.88 \times 10^{-6}$	$2.84 \times 10^{-6}$	$1.98 \times 10^{-6}$	$1.65 \times 10^{-6}$	$1.22 \times 10^{-6}$	
$\lambda_w$ , in.	0.021	0.026	0.035	0.056	0.072	
$q_w$ , lbf/ft <sup>2</sup>	4.03	2.55	1.81	2.20	1.62	
$Re_2$ , in. <sup>-1</sup>	46.70	35.43	24.65	18.61	13.76	
$S_w$	15.07	15.82	16.98	15.18	16.16	
$P_0'/P_0$	$1.847 \times 10^{-4}$	$1.454 \times 10^{-4}$	$1.028 \times 10^{-4}$	$1.787 \times 10^{-4}$	$1.313 \times 10^{-4}$	
Test Section Diameter, in.	10	11	10	7	5	

**b. SI Units**

$P_0$ , atm	19.00	15.28	15.31	10.72	10.76
$T_0$ , °K	2906	2517	2552	3711	3703
$h_0$ , J/gm	3500	2987	3033	4573	4561
$M_0$	18.01	18.91	20.29	18.14	19.32
$Re_0$ , cm <sup>-1</sup>	501	433	345	191	160
$P_w$ , N/m <sup>2</sup>	0.851	0.488	0.301	0.457	0.297
$T_w$ , °K	46.07	36.23	31.96	58.18	51.28
$U_w$ , m/sec	2493	2320	2339	2822	2821
$\rho_w$ , kg/m <sup>3</sup>	$6.22 \times 10^{-5}$	$4.55 \times 10^{-4}$	$3.17 \times 10^{-4}$	$2.64 \times 10^{-4}$	$1.95 \times 10^{-4}$
$\lambda_w$ , cm	0.053	0.066	0.089	0.142	0.183
$q_w$ , N/m <sup>2</sup>	193	122	85.7	105	77.6
$Re_2$ , cm <sup>-1</sup>	18.4	13.9	9.70	7.33	5.42
$S_w$	15.07	15.82	16.98	15.18	16.16
$P_0'/P_0$	$1.847 \times 10^{-4}$	$1.454 \times 10^{-4}$	$1.028 \times 10^{-4}$	$1.787 \times 10^{-4}$	$1.313 \times 10^{-4}$
Test Section Diameter, cm	25.4	27.9	25.4	17.8	12.7

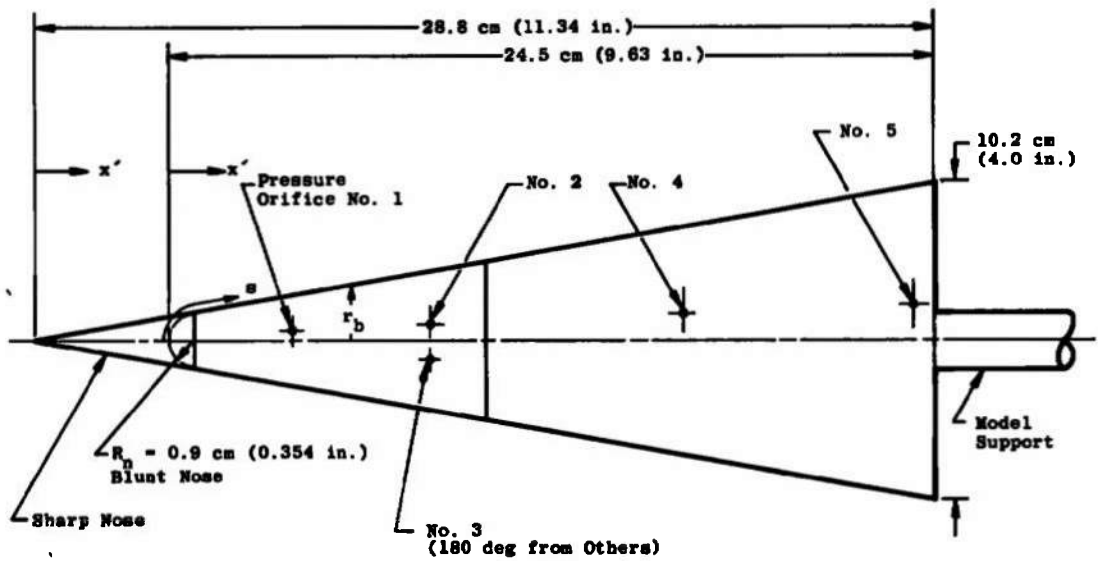


Figure 3. Model schematic.

Table 2. Pressure Orifice Schedule  
a. Sharp Nose Model

Orifice	$x'$	$s$	$r_b$
1	8.25 cm (3.25 in.)	8.37 cm (3.30 in.)	1.44 cm (0.56 in.)
2	12.62 cm (4.97 in.)	12.82 cm (5.05 in.)	2.21 cm (0.87 in.)
3	12.66 cm (4.98 in.)	12.86 cm (5.06 in.)	2.21 cm (0.87 in.)
4	20.77 cm (8.18 in.)	21.09 cm (8.30 in.)	3.64 cm (1.43 in.)
5	28.20 cm (11.10 in.)	28.63 cm (11.27 in.)	4.95 cm (1.95 in.)

b. Blunt Nose Model

1	3.91 cm (1.54 in.)	4.47 cm (1.76 in.)	1.44 cm (0.56 in.)
2	8.29 cm (3.26 in.)	8.91 cm (3.51 in.)	2.21 cm (0.87 in.)
3	8.33 cm (3.28 in.)	8.95 cm (3.52 in.)	2.21 cm (0.87 in.)
4	16.43 cm (6.47 in.)	17.18 cm (6.77 in.)	3.64 cm (1.43 in.)
5	23.86 cm (9.39 in.)	24.73 cm (9.74 in.)	4.95 cm (1.95 in.)

## 2.4 TUNNEL INSTRUMENTATION AND DATA ACQUISITION SYSTEM

In addition to instrumentation necessary to monitor the arc heater and stilling chamber conditions, the following instrumentation was used in the present test:

1. A low pressure level (3 to 30 torr full scale) pressure transducer system located within the tunnel test chamber.
2. A thermocouple system using Chromel<sup>®</sup>-Alumel<sup>®</sup> thermocouples for surface temperature measurements.

Pressure probe position and model angle of attack is varied by remotely controlled drive mechanisms and monitored by linear potentiometers.

Data were recorded on the AEDC-VKF Beckman 210 high-speed, analog-to-digital data acquisition system, which scanned all channels in about one second and recorded the data on paper tape. These raw data were then put into the AEDC-VKF CDC 1604B computer for data reduction.

## 3.0 RESULTS AND DISCUSSION

### 3.1 PROCEDURE

Both the sharp and blunt models were tested in the contoured and the conical nozzles. Angle of attack,  $\alpha$ , was varied in the range  $-10 \text{ deg} \lesssim \alpha \lesssim 10 \text{ deg}$  with data being recorded at several values of  $\alpha$ . An impact pressure probe, which was located at the model nose axial station, was moved in close to the model before each run in order to determine nozzle flow conditions. A run consisted of measuring the pressure distributions on the model at a fixed angle of attack and flow condition.

Because of an asymmetry in the model mounting system, it was not possible to obtain  $\alpha = -10 \text{ deg}$  for all flow conditions. This was caused by excessive flow blockage and resultant flow breakdown. Also, at times, for unknown reasons, the nozzle ambient or test chamber pressure would increase slightly, causing the nozzle shock to impinge on



the model and therefore prevent the obtaining of the downstream model pressures.

While the angle of attack could be determined accurately, it was not practical to obtain predetermined, repeatable values. Therefore, values of  $\alpha$  were obtained at approximately equal increments over the range where flow blockage did not occur.

It has long been recognized that whenever a temperature gradient exists along a pressure tube under rarefied flow conditions, a pressure difference will exist at the ends of the tube. This is the well-known thermal transpiration effect. For the present test, the model and therefore the pressure sensing orifice as well as the pressure measuring device were maintained at close to room temperature by means of water cooling, thereby eliminating the effect of thermal transpiration. However, it is not as widely recognized that thermal nonequilibrium at the sensing orifice can give rise to significant error. This will be discussed in the next section.

### 3.2 ORIFICE CORRECTION

It was first shown by Potter, Kinslow, and Boylan (Ref. 4) that under rarefied, nonequilibrium conditions the pressure sensed by an orifice in a surface may not indicate the true pressure existing at the surface. In a more recent paper by Kinslow and Potter (Ref. 5), a method is given for correcting pressures measured by an orifice when heat flux and shear stress are present at a surface. In order to correct the pressure data for the orifice effect, it is necessary to know the heat flux, shear stress, and thermal accommodation coefficient.

At the time of this writing, the paper presented by Kinslow and Potter (Ref. 5) had not been published. Therefore, it was decided to include the basic material in this paper as Appendix B in the present report.

The heat flux can be obtained from the heat-transfer phase of this study which was performed by Boylan (Ref. 2). Because the pressure test and the heat-transfer test were not run under exactly the same flow conditions and angle of attack and in order to eliminate the experimental scatter of the heat-transfer data, an empirical equation which best fits the data was obtained for both the sharp and blunt cones. The result obtained is

$$\dot{q} = \dot{q}_{\alpha=0} [1 + 5.015 \sin \alpha \cos \phi + 7.601 (\sin \alpha \cos \phi)^2] \quad (1)$$

where  $\dot{q}$  is the heat-transfer rate and  $\phi$  is the roll angle, and for a sharp cone

$$\dot{q}_{\alpha=0} = -0.538 \rho_{\infty} U_{\infty} h_o \bar{v}^* \sqrt{\gamma \cos \theta} \sin \theta \quad (2)$$

where  $\rho_{\infty}$  is free-stream density,  $U_{\infty}$  is free-stream velocity, and  $h_o$  is stagnation enthalpy, with  $\bar{v}^*$  based upon a reference temperature  $T^* = T_o(1/2 - \cos \theta/3) + T_w/2$ , ( $w$  is wall condition), and for a blunt cone

$$\dot{q}_{\alpha=0} = -0.636 \rho_{\infty} U_{\infty} (h_o - h_w) \sqrt{(R_n/x') \bar{v}^*} \sin \theta \quad (3)$$

where  $R_n$  is model nose radius,  $x'$  is model coordinate parallel to axis, and  $\theta$  is the local body angle, with  $T^* = T_o/6 + T_w/2$ . It should be emphasized that these results are based upon the Tunnel M heat-transfer data and therefore may not be valid outside this range.

Shear stress data have not been obtained in Tunnel M. However, Vidal and Bartz (Ref. 6) have made surface measurements, which include skin friction, on flat plates and wedges under low-density hypersonic flow conditions. It appears from their investigation that a modified form of Reynolds analogy is valid under rarefied flow conditions. An empirical expression which fits the data within the limits of the relative flow inclination angle covered in the present test is

$$C_F = 2 St \cos^{2.5} \beta Pr^{2/3} \quad (4)$$

where  $C_F$  is the skin-friction coefficient  $\tau/q_w$ ,  $St$  is the Stanton number, and  $\beta$  is the angle between the local surface normal and the undisturbed free-stream flow vector. As stated above, this expression is based upon data from flat plates and wedges. However, for lack of more direct results, it is assumed in this report that Eq. (4) is also valid for an axially symmetric body.

Substituting for  $C_F$  and  $St$  into Eq. (4), the expression for the skin friction,  $\tau$ , becomes

$$\tau = \frac{\dot{q} U_{\infty} Pr^{2/3} \cos^{2.5} \beta}{(h_o - h_w)} \quad (5)$$

The role of the thermal accommodation coefficient,  $\alpha_e$ , on the orifice effect was first investigated by Kinslow and Arney (Ref. 7). The value of  $\alpha_e$  obtained in that work from experimental measurements was 0.79 for nitrogen reflected from engineering surfaces. In the present work, it is assumed that this value is applicable.

Using these expressions for  $\dot{q}$ ,  $\tau$ , and  $\alpha_e$ , the orifice correction was made on the measured pressure,  $p_i$ , to obtain the true surface pressure,  $p_w$ . The correction varied over the range of approximately 25 to 100 percent of the measured pressure; i.e., the indicated pressure was as low as one-half the true surface pressure.

### 3.3 PRESSURE CORRECTION FOR SOURCE FLOW EFFECTS

The analysis of source flow effects on bodies at angle of attack which follows closely parallels a previous AEDC work by Dr. W. S. Norman (unpublished). However, the result obtained here is slightly different from his except for the case of a cone with the pitch axis at its apex.

The approach to obtain the source flow correction is briefly as follows. The pressure coefficient distribution on the axisymmetric body in a divergent conical flow field is obtained by the modified Newtonian formula based on some reference condition in the flow field. The pressure coefficient distribution is similarly obtained for the same body in a uniform flow field with properties identical to those at the reference point in the source flow. By assuming that the ratio of pressure coefficients for source flow and parallel flow is the same for Newtonian and non-Newtonian, the Newtonian result can be used to correct the real flow situation.

The nomenclature used in this section is shown in Fig. 4. The pitch axis of the model is located a distance  $L$  from the apparent source of the flow. This apparent source is not necessarily the apex of the geometric conical nozzle since under rarefied flow conditions the boundary layer is a nonlinear function of distance. For convenience both flow and body coordinate systems are introduced.

There are two basic source flow effects. One is the change in local flow properties caused by the expanding flow. This effect is manifest primarily in the decrease of local dynamic pressure in the flow direction. The other effect is the variation in the local flow inclination angle. Both of these effects are more pronounced for slender bodies.

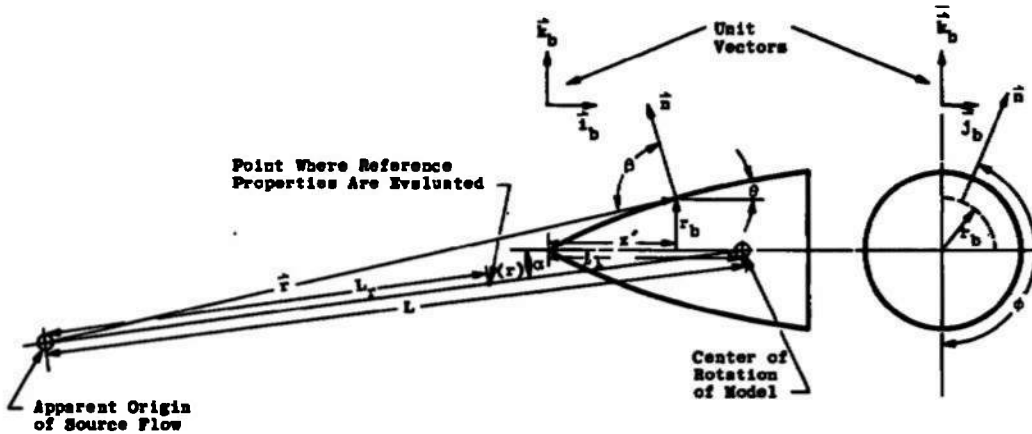


Figure 4. Body coordinate system.

The modified Newtonian expression for the local pressure coefficient is

$$C_p = C_{p_0} \cos^2 \beta \quad (6)$$

where  $\beta$  is the angle between the local surface normal and free-stream velocity vector. The pressure coefficient at a stagnation point is  $C_{p_0}$ . From vector analysis  $\cos \beta$  is given by

$$\cos \beta = \vec{n} \cdot \vec{r} / |\vec{r}| \quad (7)$$

From Fig. 4, the vectors  $\vec{n}$  and  $\vec{r}$  are given by

$$\vec{n} = -\sin \theta \vec{i}_b + \cos \theta \sin \alpha \vec{j}_b - \cos \theta \cos \alpha \vec{k}_b \quad (8)$$

$$\vec{r} = (L \cos \alpha - \ell_1 + x') \vec{i}_b + r_b \sin \phi \vec{j}_b + (L \sin \alpha - r_b \cos \theta) \vec{k}_b \quad (9)$$

Substituting Eqs. (8) and (9) into Eq. (7) and squaring yields

$$\cos^2 \beta = \frac{\{-(\sin \theta \cos \alpha + \sin \alpha \cos \theta \cos \phi) + [(\ell_1 - x')/L] \sin \theta + (r_b/L) \cos \theta\}^2}{1 + (r_b/L)^2 - 2[(\ell_1 - x')/L] \cos \alpha - 2(r_b/L) \sin \alpha \cos \phi + [(\ell_1 - x')/L]^2} \quad (10)$$

where  $r_b$  is local body radius,  $x'$  is the model coordinate parallel to axis, and  $\ell_1$  is distance from model tip to center of rotation. Let the pressure coefficient defined by using the reference quantities be denoted by a prime. Thus

$$C'_p = (p - p_{\infty}) / q_r \quad (11)$$

or in terms of the local pressure coefficient

$$C'_p = C_{p\ell} \frac{q_\infty}{q_r} + \frac{P_{\infty r}}{q_r} \left( \frac{P_\infty}{P_{\infty r}} - 1 \right) \quad (12)$$

For isentropic source flow with constant ratio of specific heats,  $\gamma$ , the following are obtained:

$$\frac{q_\infty}{q_r} = (L_r/r)^2 [1 + 2/(\gamma - 1)M_r^2]^{1/2} / [1 + 2/(\gamma - 1)M_\infty^2]^{1/2} \quad (13)$$

and

$$P_{\infty r}/q_r = 2/\gamma M_r^2 \quad (14)$$

where  $L_r$  is the distance from apparent origin of source flow to reference point. Since the term containing the static pressure in Eq. (12) is small, a first-order estimate of the pressure ratio is adequate. Assuming constant flow velocity, expanding the isentropic relation into a series containing only first-order terms the pressure ratio becomes, for  $r_b \ll L$  and small  $\alpha$ ,

$$\frac{P_\infty}{P_{\infty x}} = 1 + 2\gamma[(L_r - L/L_r) + ((\ell_1 - x')/L_r) \cos \alpha + (r_b/L_r) \sin \alpha \cos \phi] \quad (15)$$

where  $P_\infty$  is free-stream static pressure. Substituting Eqs. (6), (13), (14), and (15) into Eq. (12) yields

$$C'_p = C_{p_o} \cos^2 \beta \left( \frac{L_r}{r} \right) \sqrt{\frac{1 + 2/[(\gamma - 1)M_r^2]}{1 + 2/[(\gamma + 1)M_\infty^2]}} + \frac{4}{M_r^2} \left[ \left( \frac{L_r - L}{L_r} \right) + \left( \frac{\ell_1 - x'}{L_r} \right) \cos \alpha + \frac{r_b}{L_r} \sin \alpha \cos \phi \right] \quad (16)$$

Using Eqs. (9) and (10), Eq. (16) becomes, for large Mach number,

$$C'_p = C_{p_o} \left( \frac{L_r}{L} \right)^2 \frac{\left[ -(\sin \theta \cos \alpha + \sin \alpha \cos \theta \cos \phi) + \left( \frac{\ell_1 - x'}{L} \right) \sin \theta + \frac{r_b}{L} \cos \theta \right]^2}{\left[ 1 + \frac{r_b^2}{L^2} - 2 \left( \frac{\ell_1 - x'}{L} \right) \cos \alpha - 2 \frac{r_b}{L} \sin \alpha \cos \phi + \left( \frac{\ell_1 - x'}{L} \right)^2 \right]^2} \quad (17)$$

For the case of parallel uniform flow ( $L_r \rightarrow L \rightarrow \infty$ ) Eq. (17) reduces to the following

$$C_{p_\infty} = C_{p_o} [\sin \theta \cos \alpha + \sin \alpha \cos \theta \cos \phi]^2 \quad (18)$$

$C_{p\_}$  is the pressure coefficient in an equivalent parallel flow condition.

Equation (17) is plotted in Figs. 5 and 6 for a 10-deg, half-angle sharp cone with  $C'_p/C_{p0}$  given as a function of angle of attack,  $\alpha$ , for various positions,  $x'$ , on the body. The result for the pitch axis at the apex is given in Fig. 5, while Fig. 6 gives the results for the same body with the pitch axis located at a point where  $l_1/L = 0.2$ . Equation (18) appears on Fig. 5 as the curve  $x'/L_r = 0$ . The ratio of Eq. (17) to Eq. (18) is shown in Figs. 7 and 8 for the same 10-deg cone as given previously. Note that in Fig. 7 the ratio of the pressure coefficient for the source flow Newtonian and the uniform flow Newtonian is almost independent of angle of attack for the pitch axis at the model apex, whereas from Fig. 8 the same ratio is a strong function of  $\alpha$ . In other words, with the pitch axis downstream of the apex the effect of the local flow angularity is magnified for the Newtonian pressure coefficient.

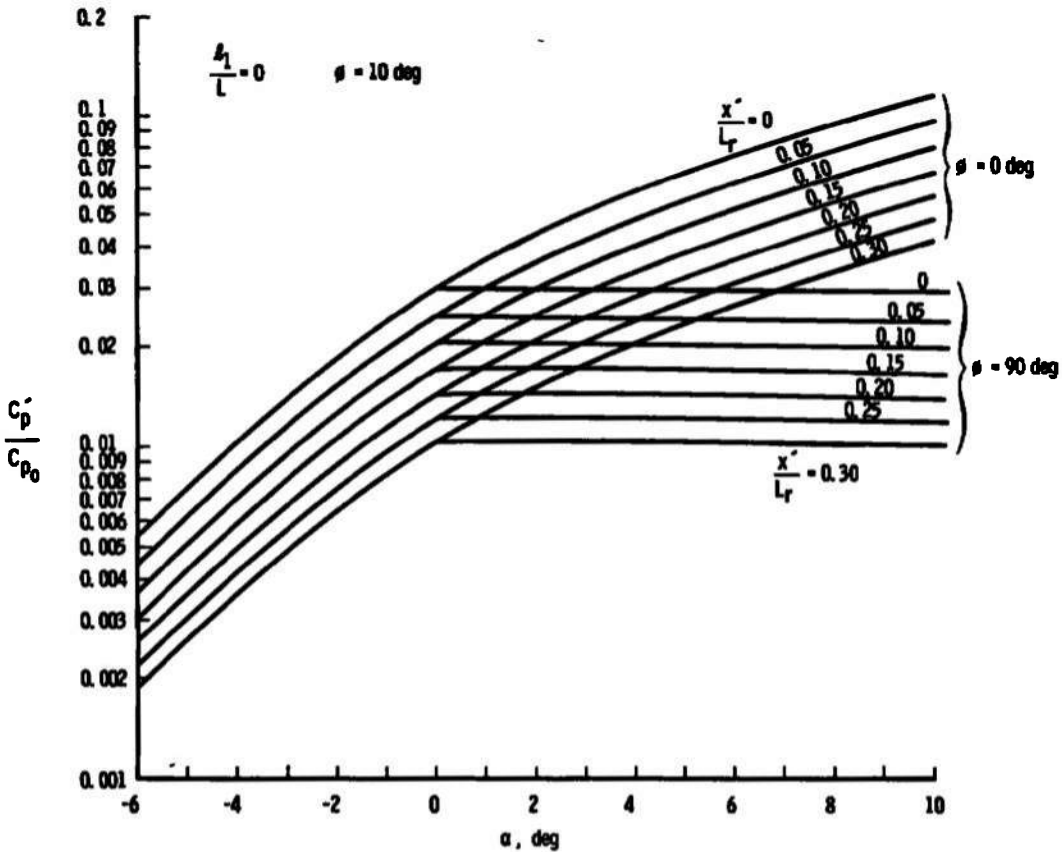


Figure 5. Plot of Eq. (17) for  $l_1/L = 0$ .

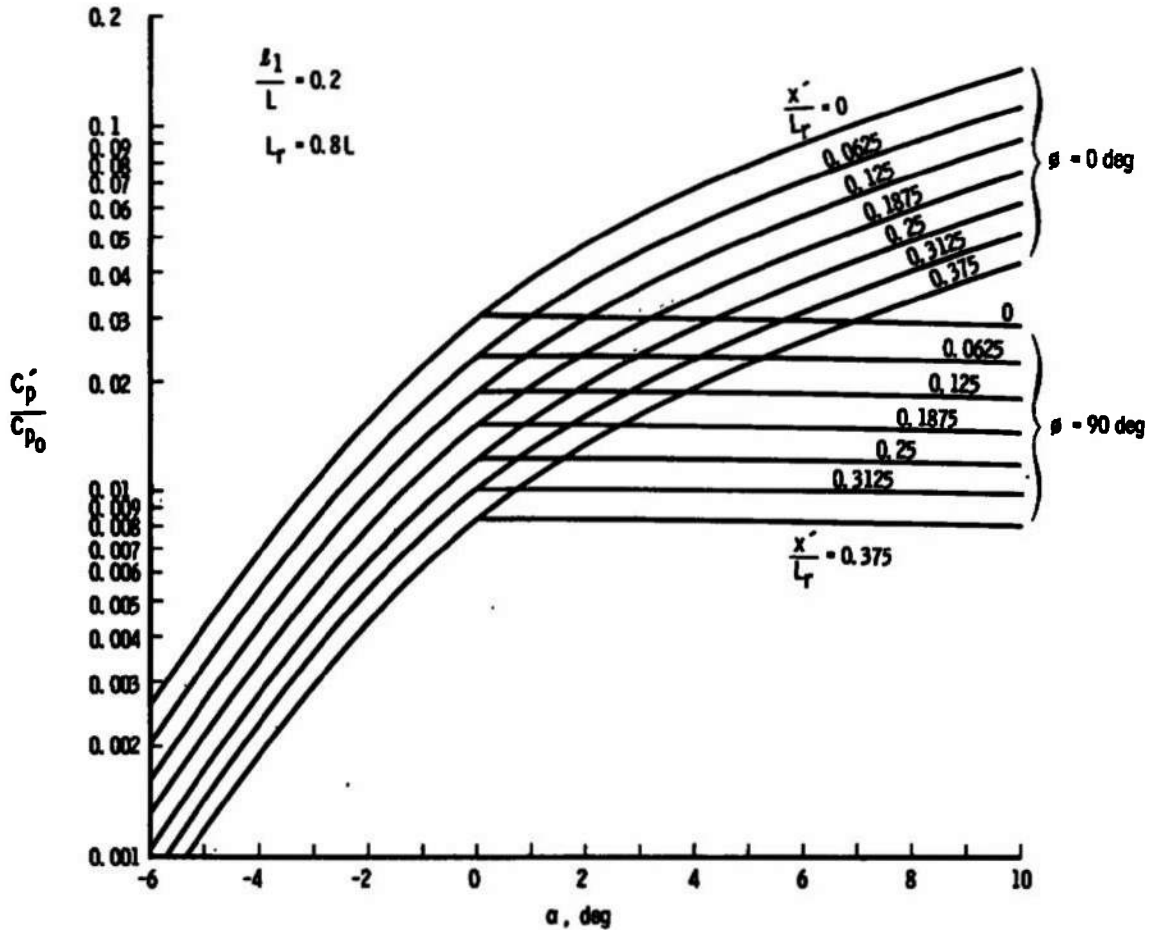


Figure 6. Plot of Eq. (17) for  $l_1/L = 0.2$ .

In order to separate the effect of flow angularity and free-stream flow gradient, the results presented in Figs. 7 and 8 are normalized to the ratio at  $x' = 0$  and shown in Fig. 9. The results for various model parameters fall within the indicated band. The analytical results of Eqs. (17) and (18) can be simplified for the special case of  $\alpha = 0$  for a sharp cone with the reference point at the apex. The result is:

$$\frac{C_p/C_{p_{\infty}}}{(C_p/C_{p_{\infty}})_{x'=0}} = \left[ 1 + 2 \frac{x'}{L_r} + \left( \frac{x'}{L_r} \right)^2 \cos^2 \theta \right]^{-2} \quad (19)$$

The results presented in Fig. 9 show that the Newtonian pressure coefficient in source flow needs to be increased by as much as a factor of over 300 percent to obtain the parallel flow value for the condition considered.

Also shown in Fig. 9 is the result of a method-of-characteristics calculation for the surface pressure coefficient on a 10-deg cone in source flow with a Mach number at the model apex of 20.

The effect of angle of attack can be better seen if the results presented in Figs. 5 and 6 are normalized to the value at zero angle of attack. The result of this is shown in Fig. 10. Notice that this ratio is

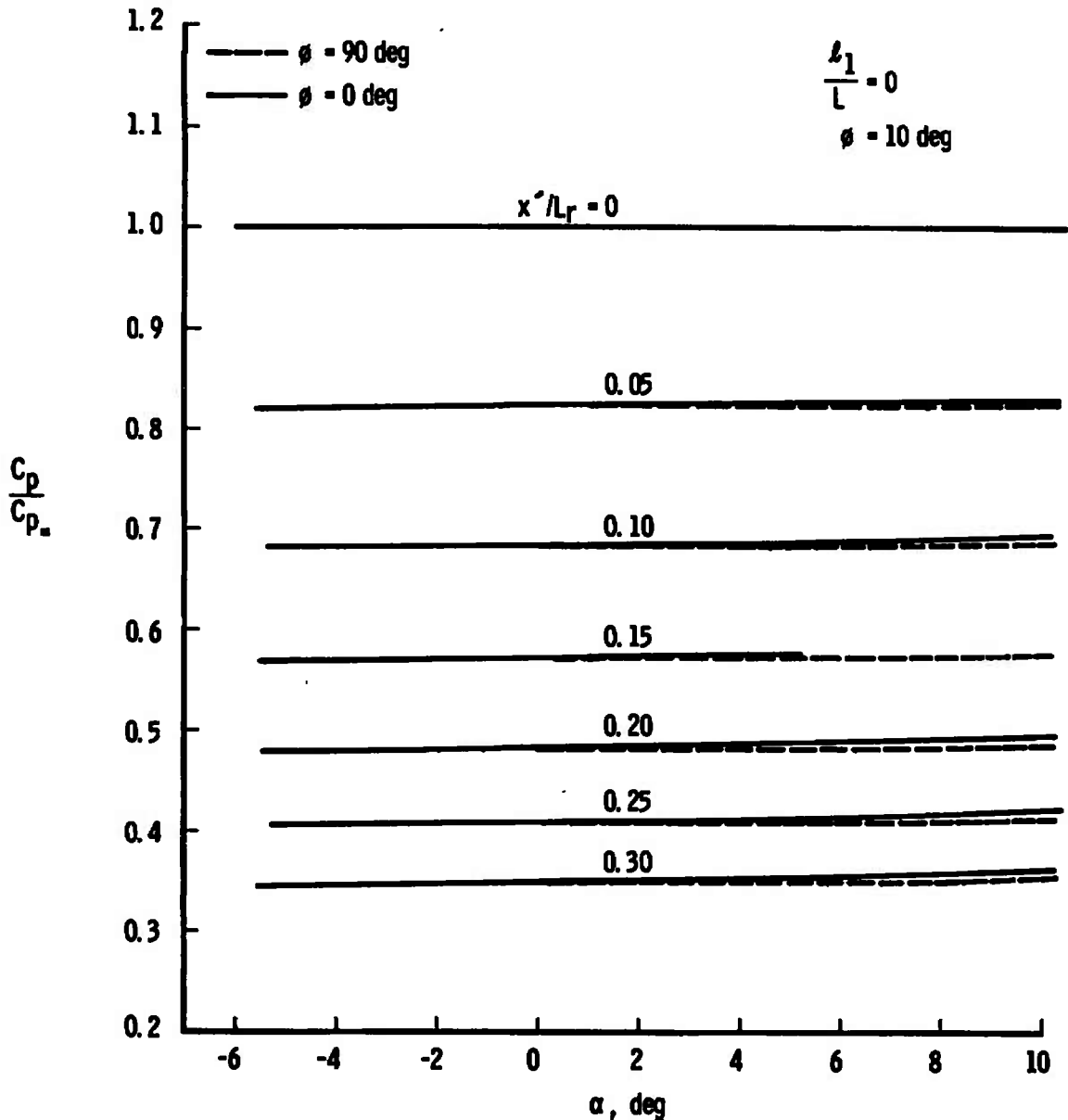


Figure 7. Ratio of uniform and source flow pressure coefficient for  $l_1/L = 0$ .



primarily a function of  $l_1/L_r$  and  $\phi$ , while the variation with  $x'/L_r$  is of secondary importance. However, the dependence upon  $l_1/L$  is less than the order of 20 percent for the conditions considered for  $\phi = 0$  deg and is negligible for  $\phi = 90$  deg. In other words, the influence of source flow on the effect of angle of attack is considerably less than the effect of axial flow gradient as shown in Fig. 9.

As stated earlier, the Newtonian source results summarized in Figs. 9 and 10 will be used as a basis for the correction of experimental results which are presented later.

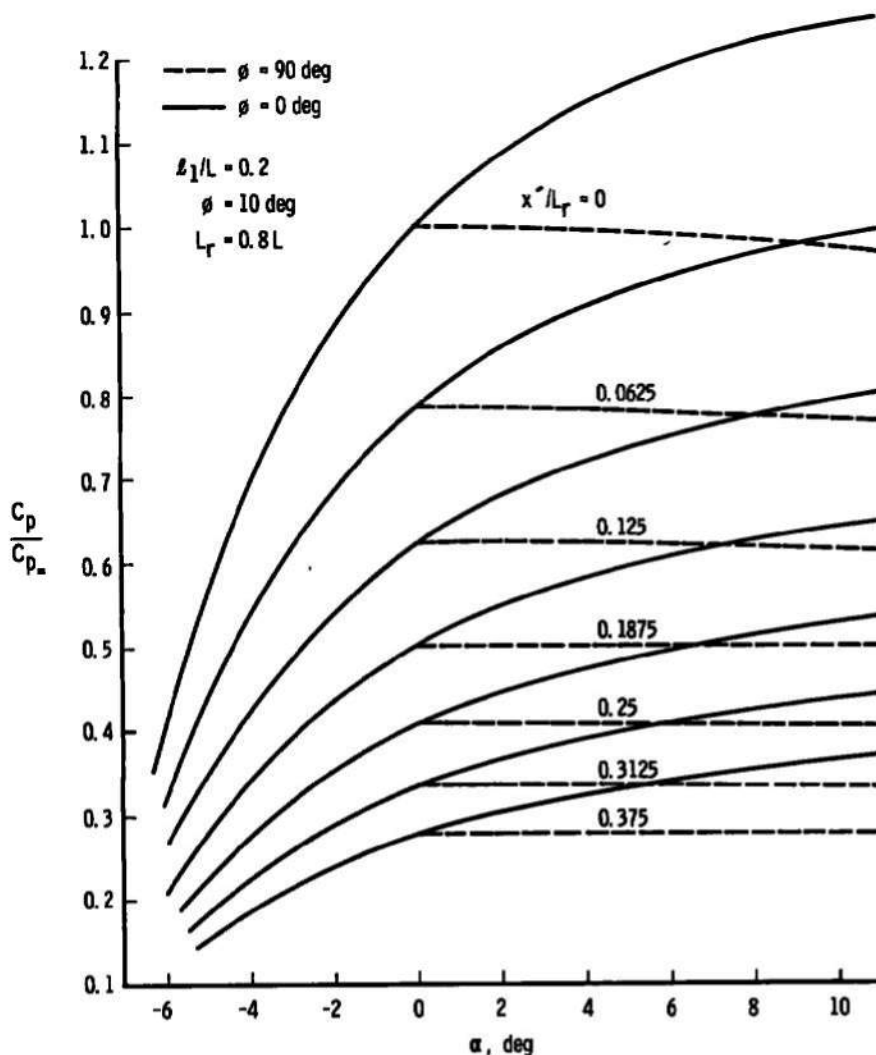


Figure 8. Ratio of uniform and source flow pressure coefficient for  $l_1/L = 0.2$ .

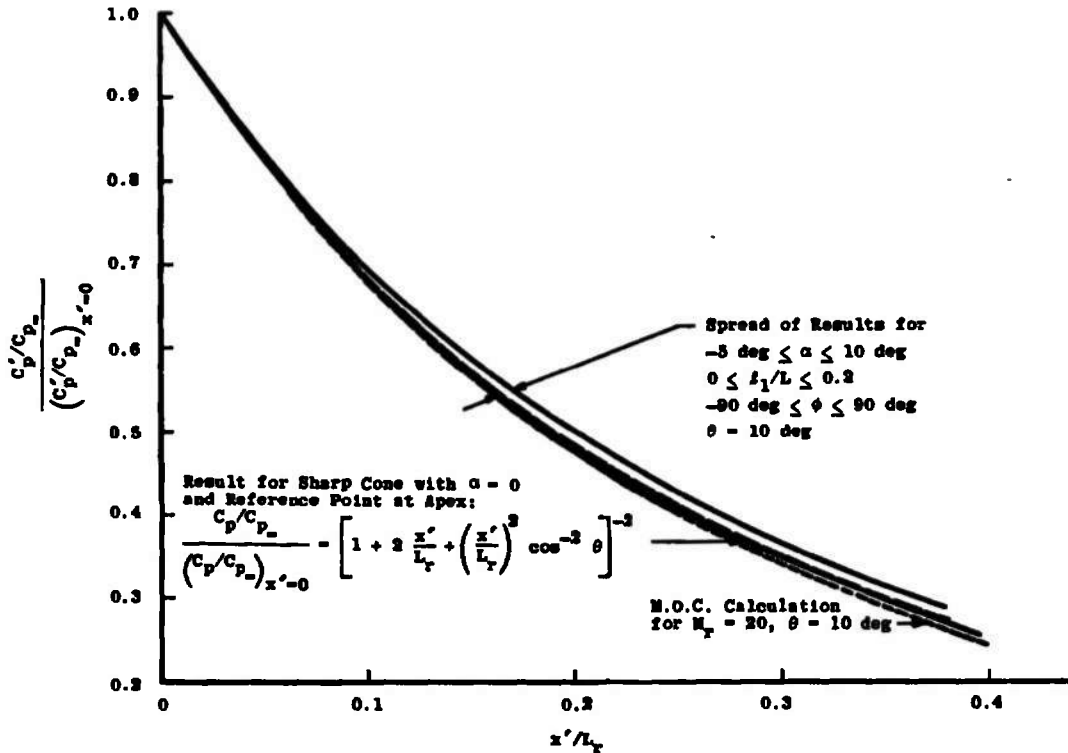


Figure 9. Normalized axial source flow effect.

### 3.4 EXPERIMENTAL RESULTS

#### 3.4.1 Sharp Cone

Figures 11 through 18 present the results of the tests on the sharp cone with  $C_p'$  as a function of  $\alpha$ . The pressure coefficient is based upon the corrected surface pressure, as discussed in Section 3.2, and local flow conditions at the model nose. Because of curtailment in tunnel test time, it was not possible to complete the proposed test matrix, e.g., tests downstream of the nozzle exit for the conical nozzle was limited to the sharp cone for  $\phi = 90$  deg and 270 deg only.

The experimental results presented in Figs. 11 through 18 are a function of Reynolds number, based upon distance along the cone, and they contain the effects of source flow. In an attempt to minimize the effect of Reynolds number, the data are normalized with respect to the zero-angle-of-attack value. These results are shown in Fig. 19 for the contoured nozzle and in Fig. 20 for the two-flow conditions in the conical nozzle. Notice that individual data points are not shown; only a band is given to represent the limits of the measurements.

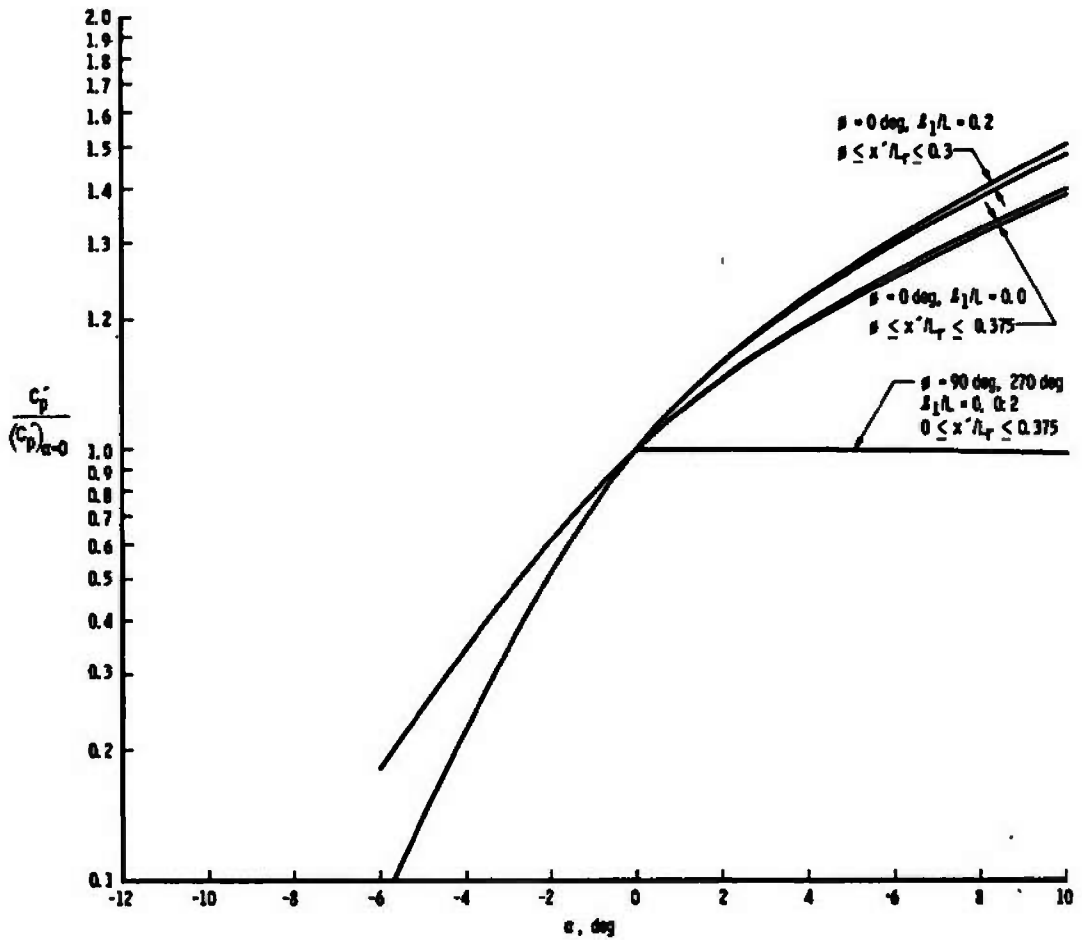


Figure 10. Variation of Newtonian pressure coefficient ratio with angle of attack.

From Table 1 the unit Reynolds numbers at the exit of the conical nozzle for Conditions I and II are  $1100 \text{ in.}^{-1}$  and  $486 \text{ in.}^{-1}$ , respectively. It is to be expected, as can be seen from Fig. 20, that the variation in pressure coefficient with angle of attack is less at the lower Reynolds numbers. This effect was not unexpected since at the lower Reynolds number the boundary layer is thicker and a given change in angle of attack changes the effective body angle a smaller proportion. Of course the pressure coefficient is increased at the lower Reynolds number condition, but this effect is eliminated in the ratio shown in Fig. 20.

The results of the Newtonian pressure coefficient for parallel and source flow as given in Fig. 10 can be compared directly with the experimental results as presented in Figs. 10 and 20. Notice that the

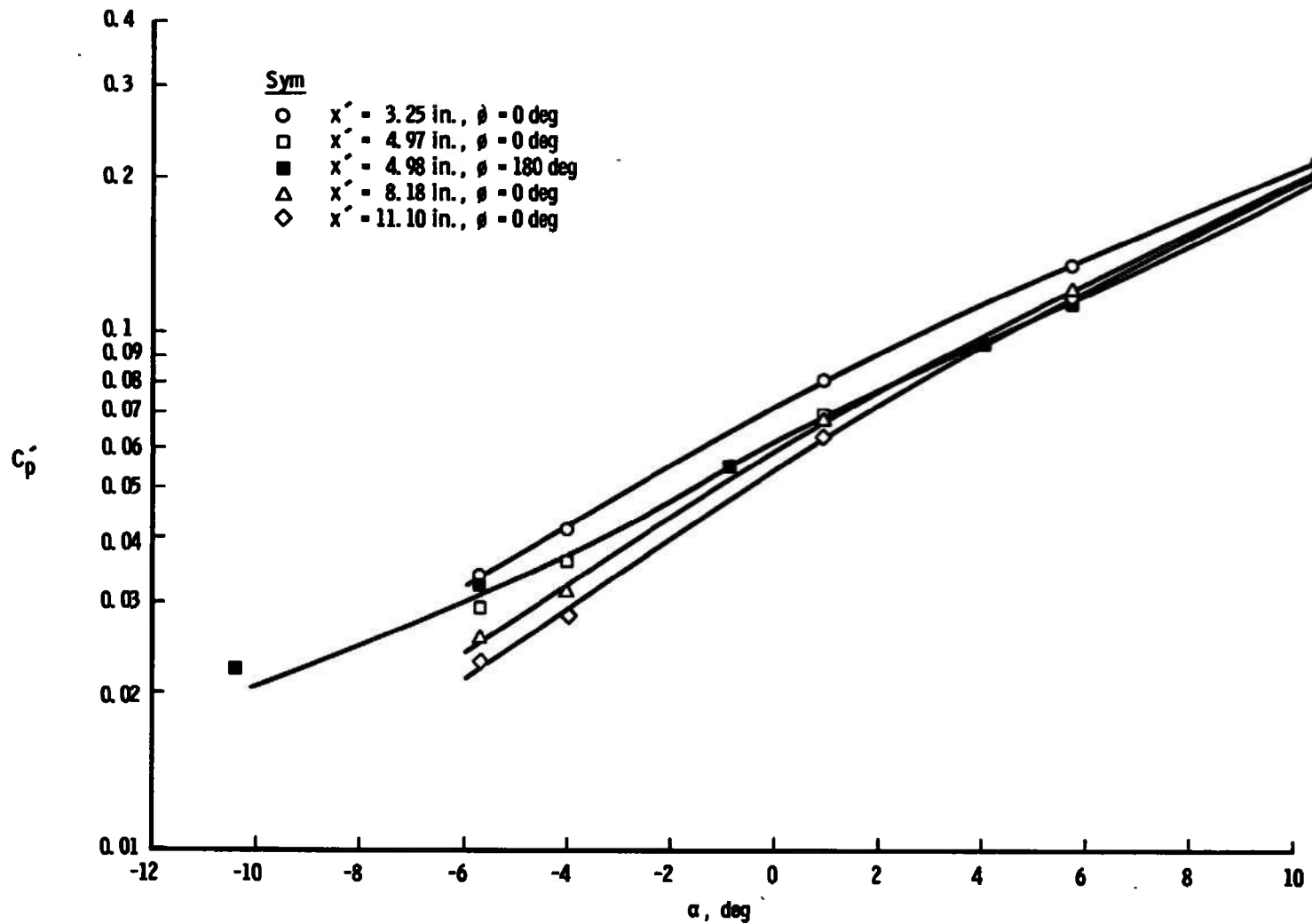


Figure 11. Sharp cone experimental pressure coefficient in the contoured nozzle for  $\phi = 0, 180$  deg.

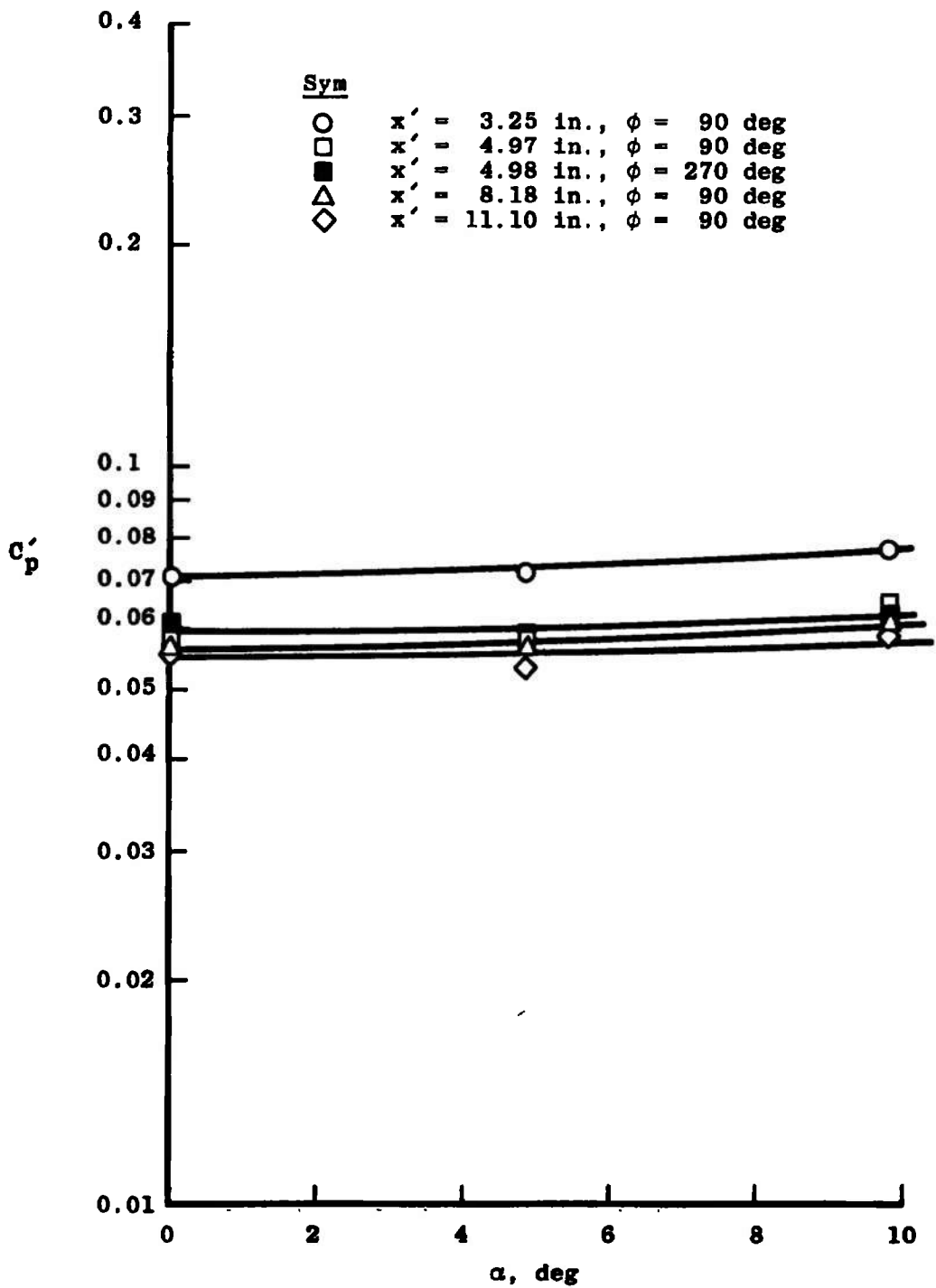


Figure 12. Sharp cone experimental pressure coefficient in the contoured nozzle for  $\phi = 90$  deg,  $270$  deg.

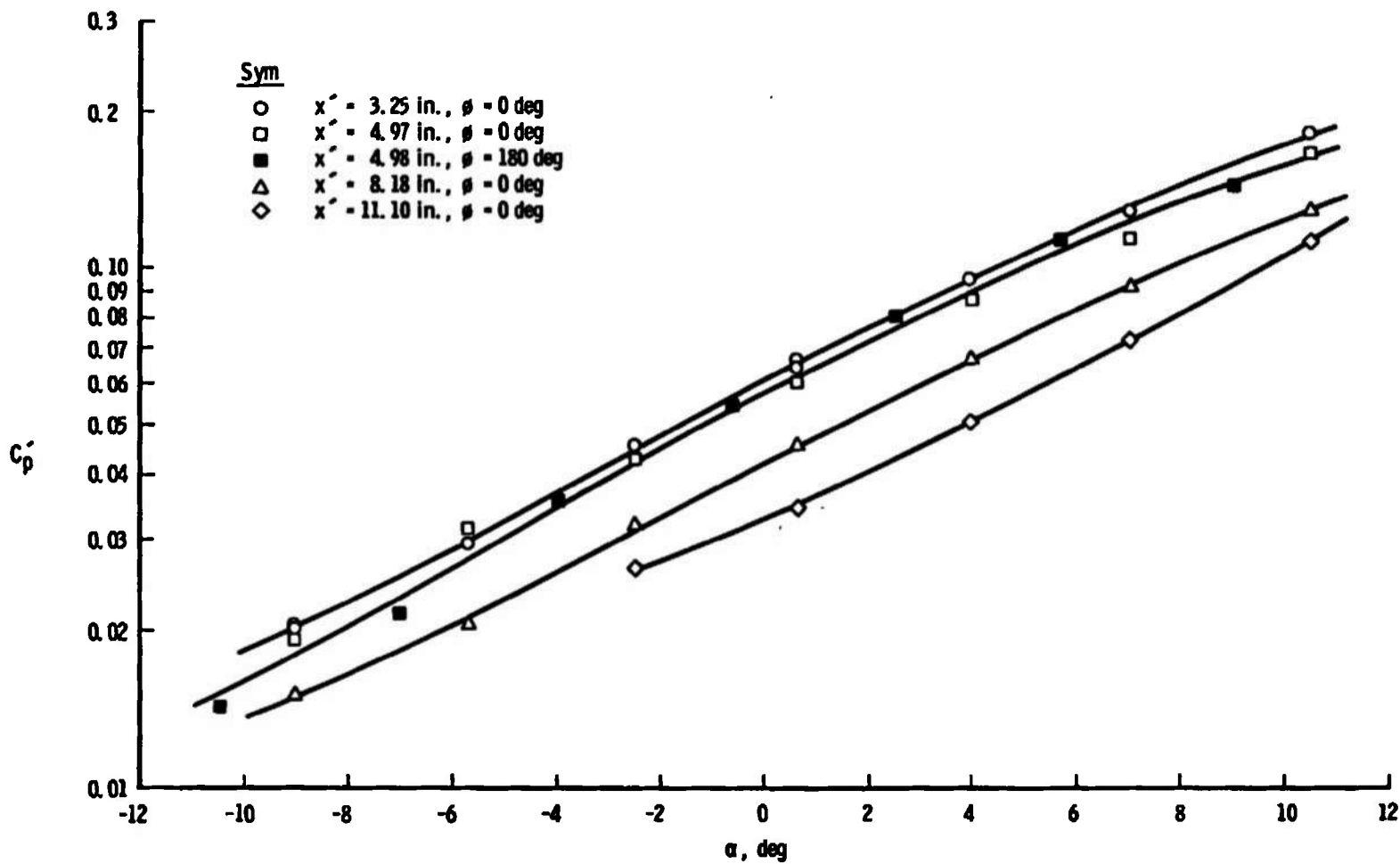


Figure 13. Sharp cone experimental pressure coefficient for Condition I in the conical nozzle for  $x = 0$  and  $\phi = 0, 180$  deg.

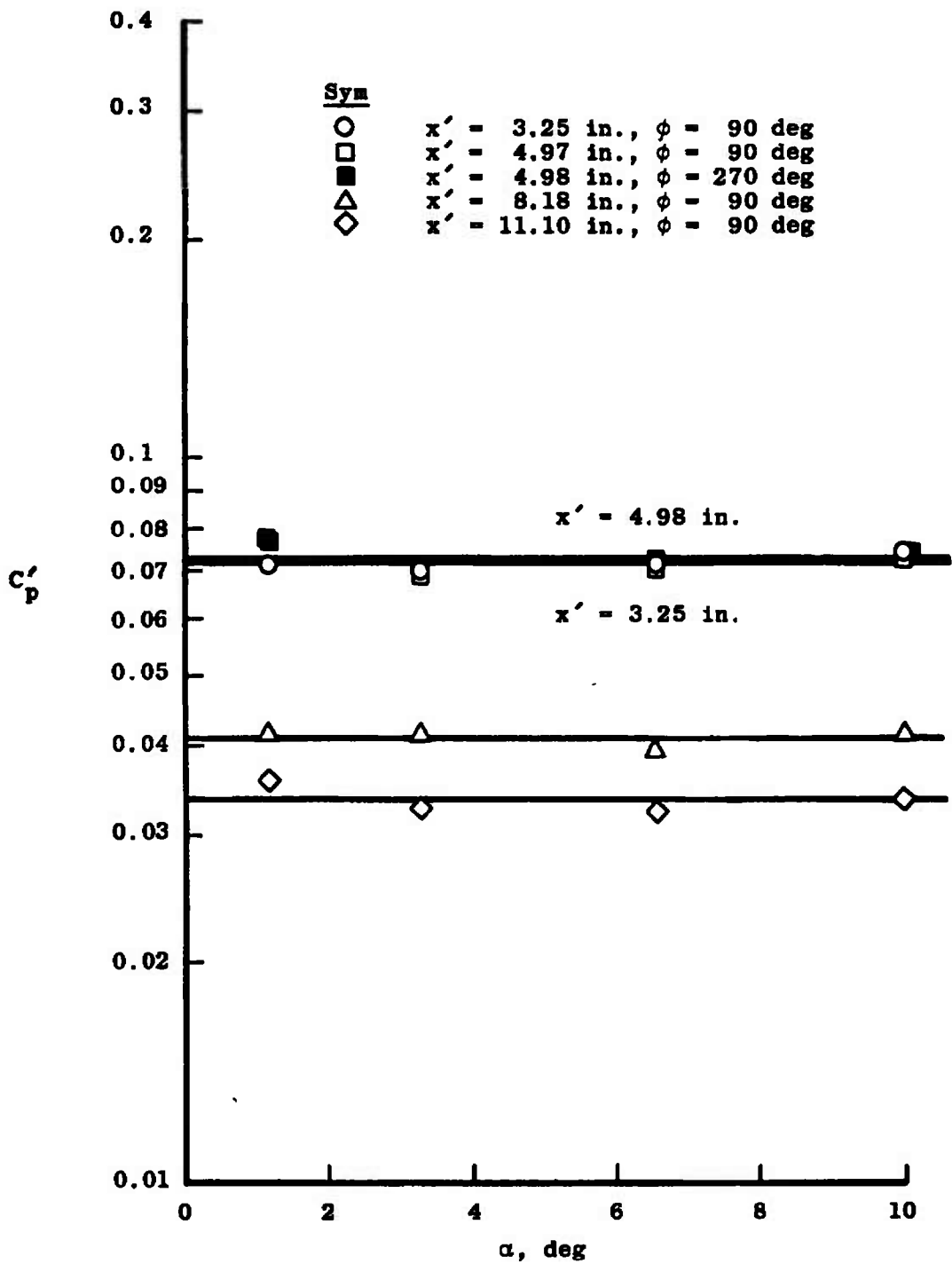


Figure 14. Sharp cone experimental pressure coefficient for Condition I in the conical nozzle for  $x = 0$  and  $\phi = 90$  deg, 270 deg.

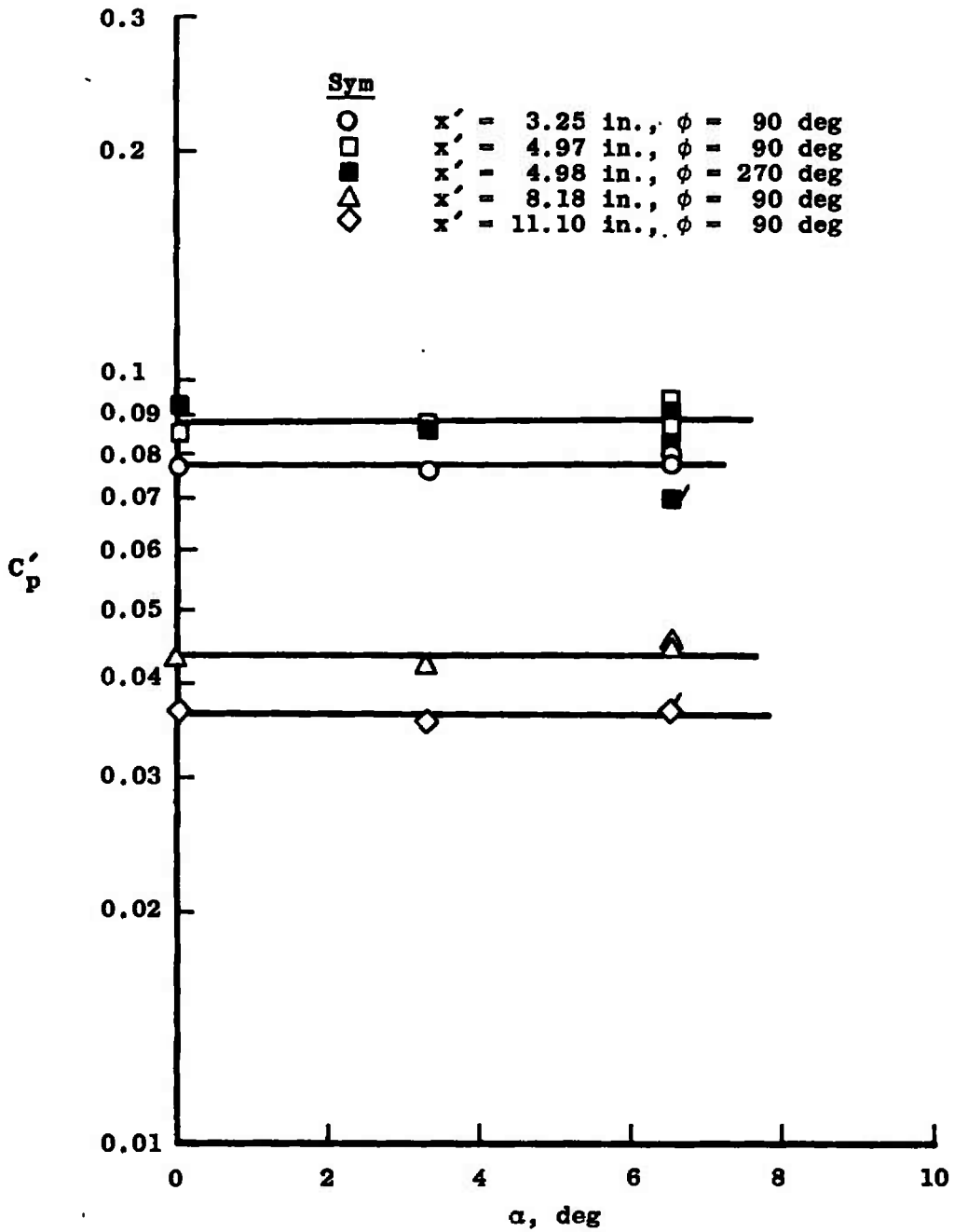


Figure 15. Sharp cone experimental pressure coefficients for Condition I in the conical nozzle for  $x = 12$  in. and  $\phi = 90$  deg, 270 deg.



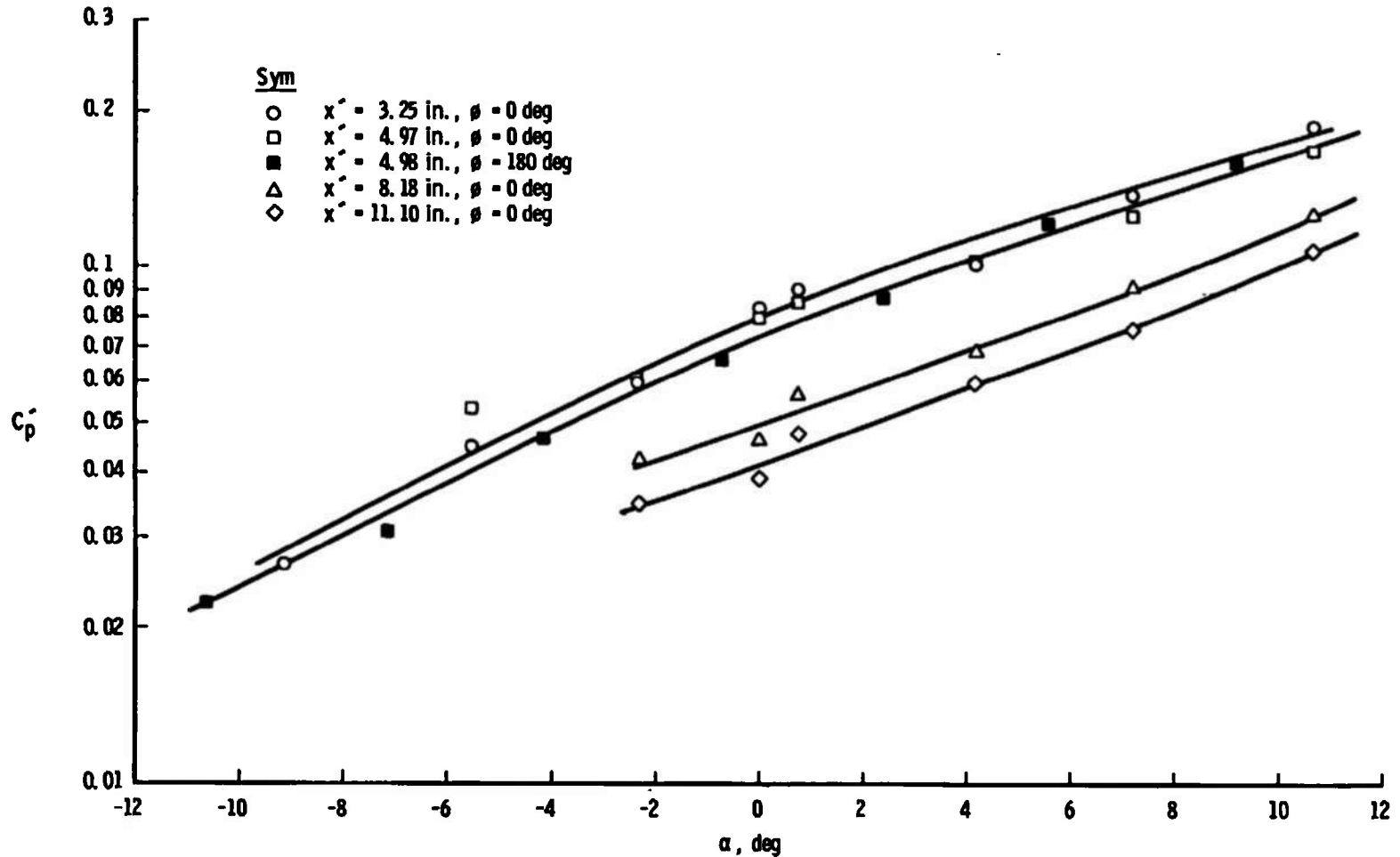


Figure 16. Sharp cone experimental pressure coefficient for Condition II in the conical nozzle for  $x = 0$  and  $\phi = 0, 180$  deg.

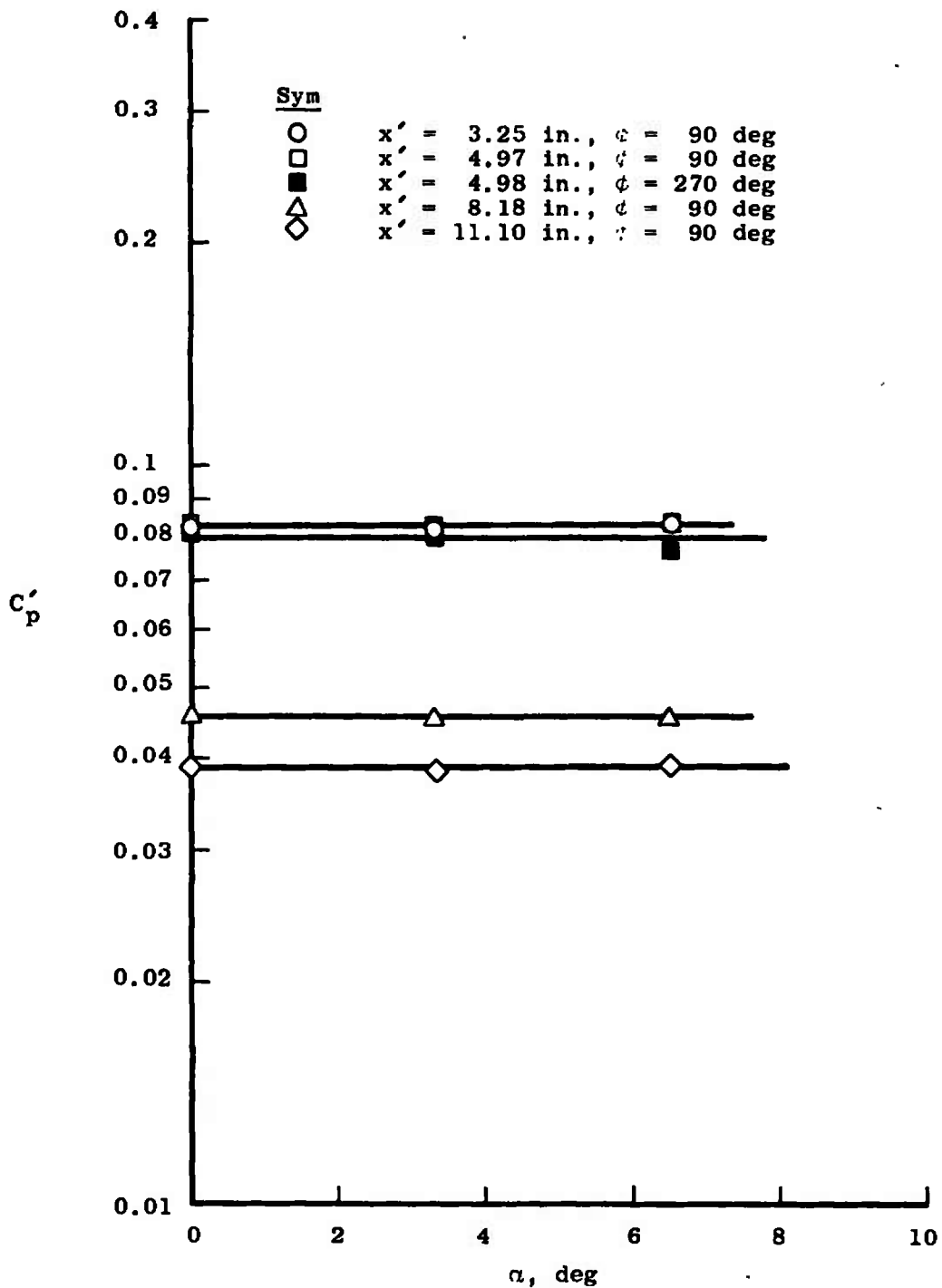


Figure 17. Sharp cone experimental pressure coefficient for Condition II in the conical nozzle for  $x = 0$  and  $\phi = 90$  deg,  $270$  deg.

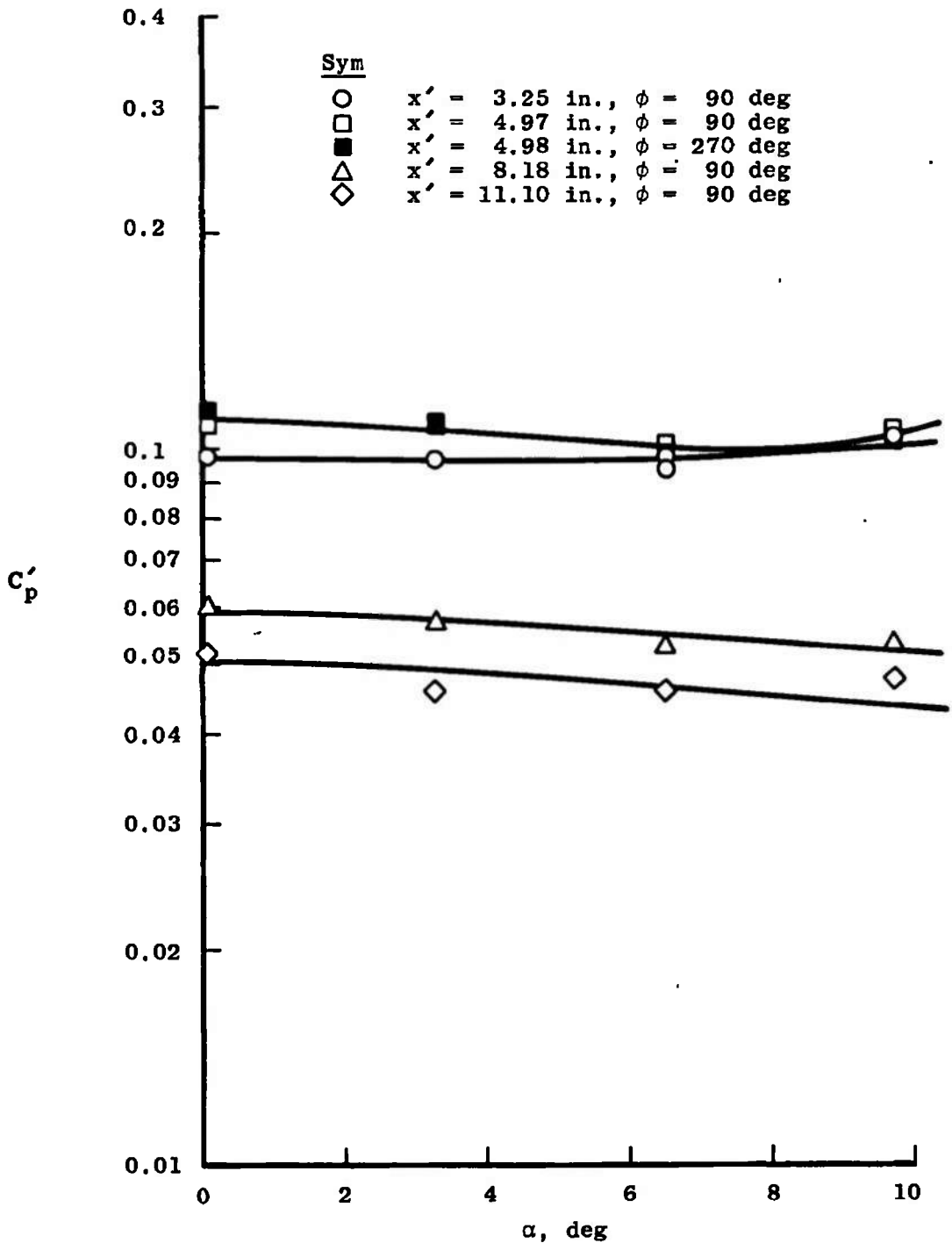


Figure 18. Sharp cone experimental pressure coefficient for Condition II in the conical nozzle for  $x = 12$  in. and  $\phi = 90$  deg, 270 deg.

variation of the pressure coefficient ratio for the Newtonian is considerably greater than for the data. This result is in line with the argument just given for the variation with Reynolds number since the Newtonian is the limit for no boundary layer at high Mach number. In fact, the Newtonian value approaches zero at  $\alpha = -10$  deg for the parallel flow case and at  $\alpha > -10$  deg for the source flow condition. The effect of the boundary layer is more pronounced at lower (more negative) angles of attack since for this configuration the pressure is less and therefore the boundary layer is thicker than at the larger angle of attack.

Returning now to the determination of the effect of source flow on the experimental data, compare the results from the contoured nozzle (Fig. 19) and the results from Condition I in the conical nozzle (Fig. 20). The Reynolds numbers for these two conditions are  $1272 \text{ in.}^{-1}$  and  $1100 \text{ in.}^{-1}$ , respectively. Based upon Reynolds number, the results for

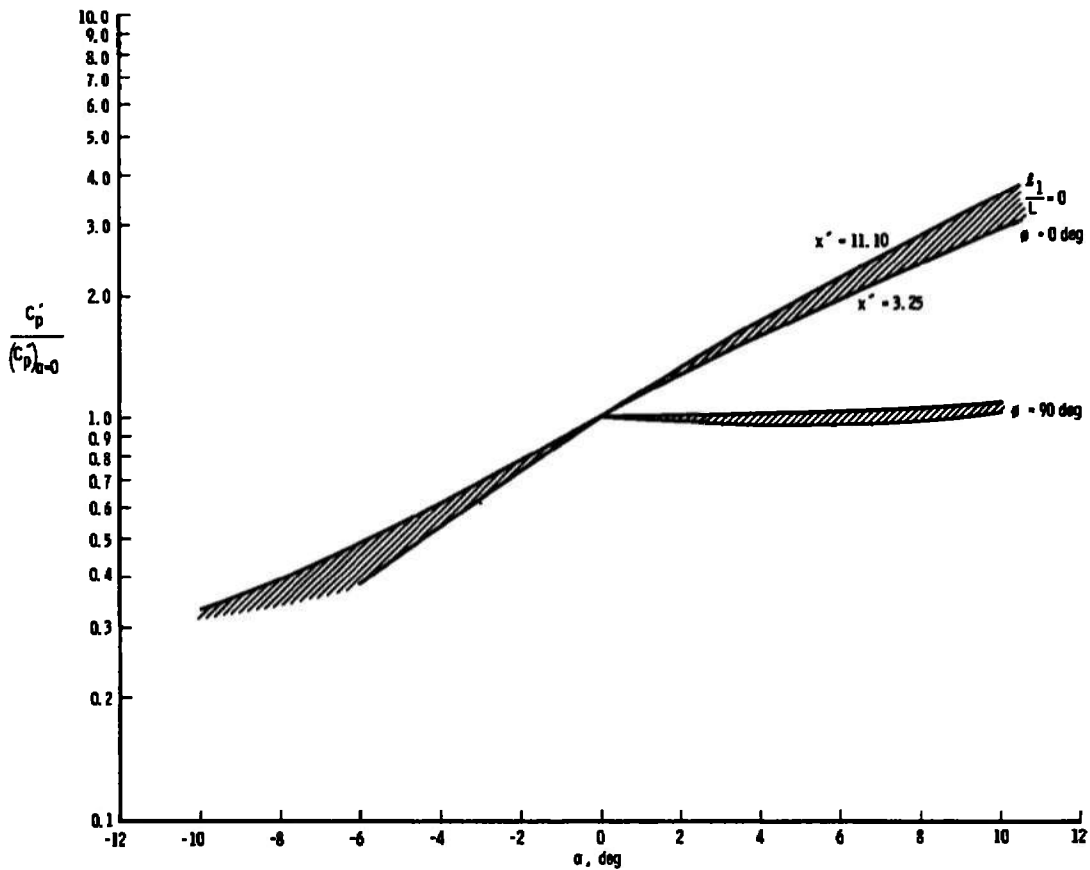


Figure 19. Experimental variation of pressure coefficient ratio with angle of attack for the sharp cone in the contoured nozzle.

the source flow condition should be lower at positive angle of attack than the parallel flow conditions. However, based upon the Newtonian source flow analysis (Fig. 10), the results for the source flow should be slightly above parallel flow values. Looking now at the experimental results, it can be seen that the parallel flow results are slightly above the source flow result for Condition I. This fact indicates that the effect of Reynolds number overshadows the source flow effect. It can be concluded that since the Reynolds number is only slightly different, the effect of source flow is a negligible influence on the variation of pressure coefficient with angle of attack under the present flow conditions.

In order to ascertain the source flow effect on the model axial pressure distribution, the data will be examined in more detail for the case of  $\alpha = 0$ . Extensive theoretical (Refs. 8 through 11) and experimental (Refs. 12 through 19) studies have been previously made of sharp cones

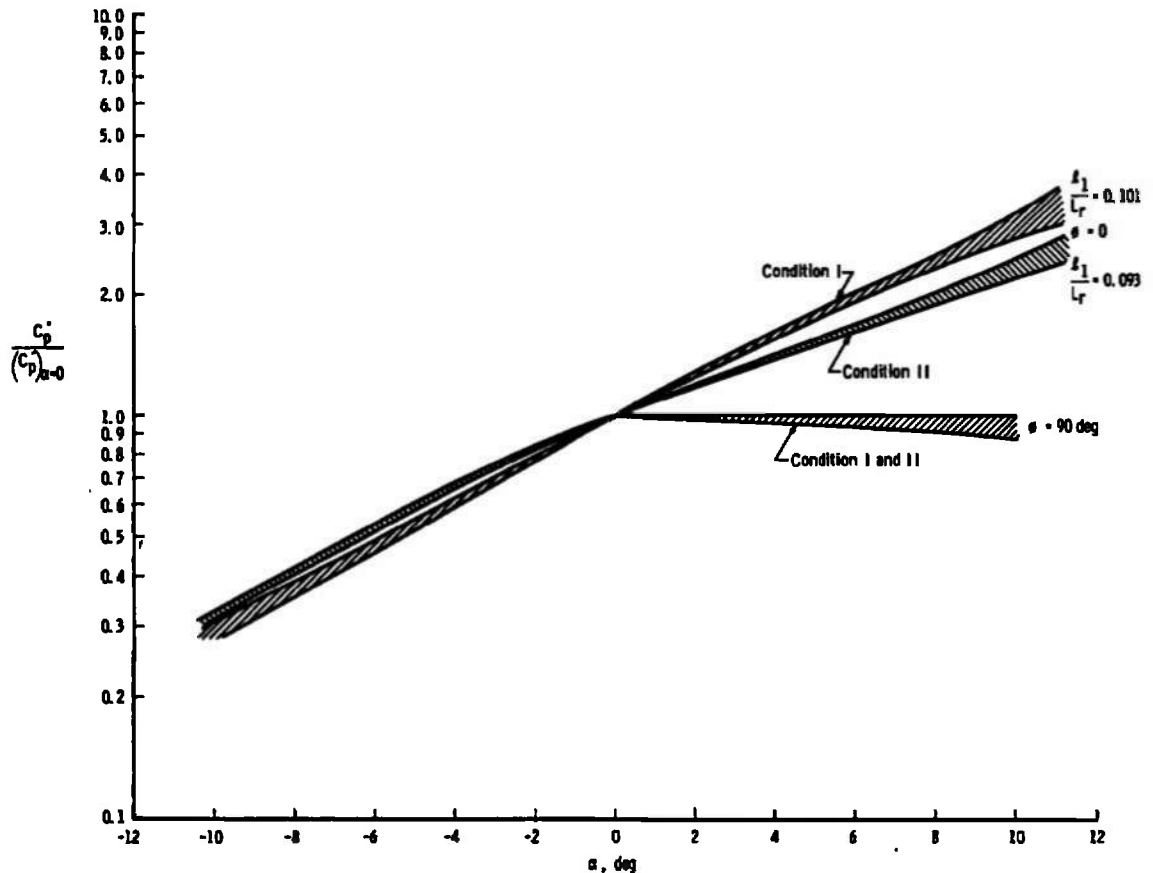


Figure 20. Experimental variation of pressure coefficient ratio with angle of attack for the sharp cone in the conical nozzle.

at zero angle of attack. In order to make comparison of the present data for  $\alpha = 0$ , the data as a function of  $\alpha$  are interpolated to obtain these values. For sharp cones, surface pressure is usually presented as a ratio to the inviscid, high Reynolds number pressure,  $p_{inv}$ . The ratio of  $p_{inv}$  to  $p_{\infty}$  has been calculated by Sims (Ref. 20) for Mach numbers up to 20. Additional calculations for  $M > 20$  were performed by Sims for Vas and reported in Ref. 18. These values of  $p_{inv}/p$  are shown in Fig. 21 as a function of Mach number for a 10 deg half-angle sharp cone.

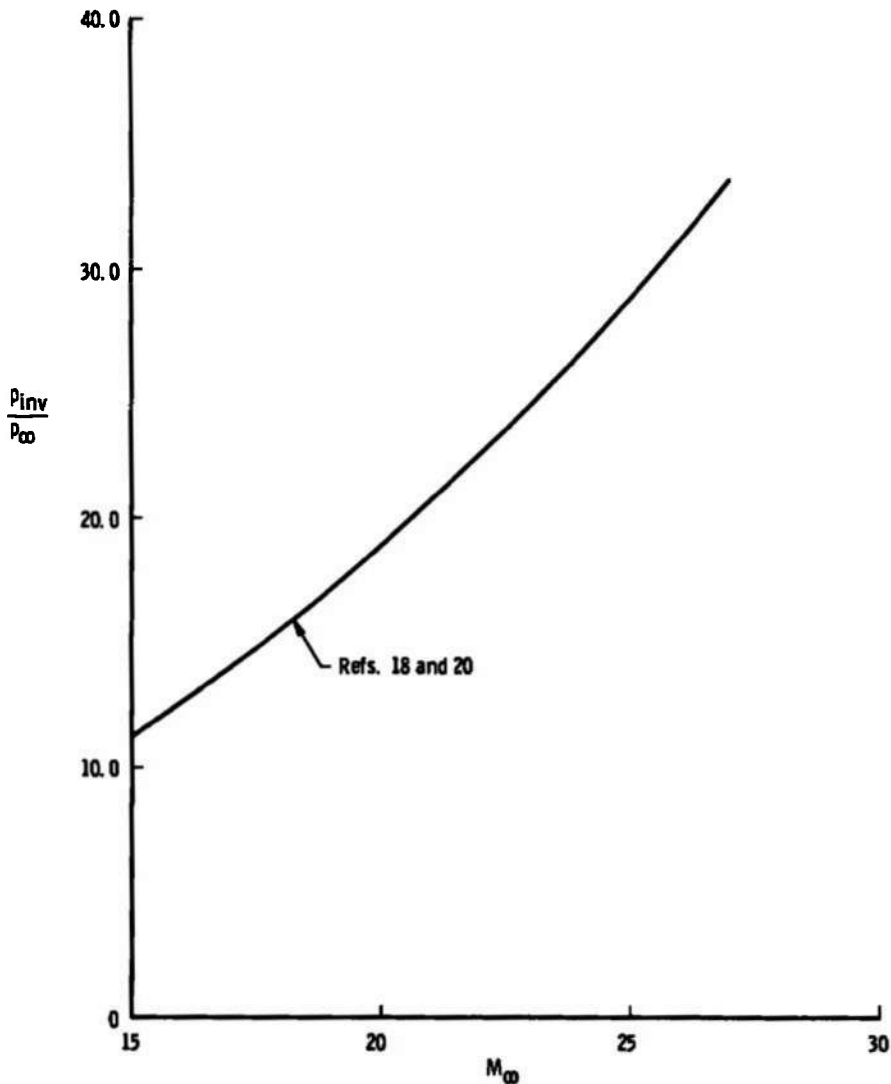


Figure 21. Calculated inviscid pressure on 10-deg sharp cone.

The ratio of the experimental surface pressure, corrected for the orifice effect, to the inviscid surface pressure is shown in Fig. 22. Also shown are previous experimental results, which were obtained under conditions where test section flow gradients were negligible. Notice that the present results for the contoured nozzle agree fairly well with previous data, whereas the conical nozzle results are low at the small value of similarity parameter  $\bar{v}/\sin^2 \theta$  and seem to have a greater slope. Based upon the results for the Newtonian source flow as presented in Fig. 9, it can be seen that the behavior of the data taken under source flow conditions is qualitatively the same.

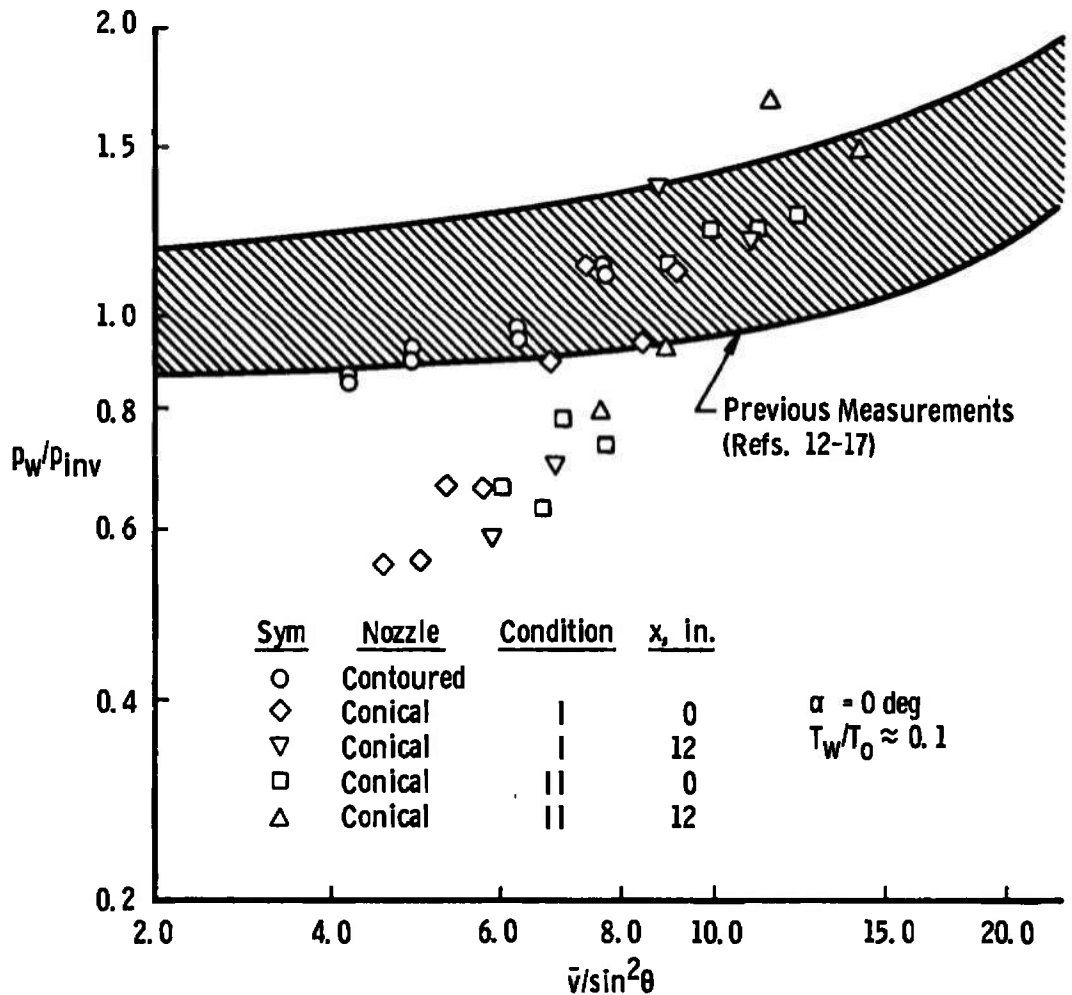


Figure 22. Sharp cone surface pressure measurements under uniform and source flow conditions.

As stated earlier, it is assumed that the results for the ratio of the surface pressure coefficient for source and uniform flow are the same for both the Newtonian calculation and the actual test condition. Applying this result for  $\alpha = 0$  as given by Eq. (19), the experimental results can be corrected to uniform flow conditions. Figure 23 gives the results of this correction, where  $p_w$  is the wall pressure corrected for source flow effects. It can be seen that the present results for parallel and source flow are in agreement when corrected in this manner. Also shown is the result of previous measurements, as shown on Fig. 23. Included too is the result of several theories based upon the assumptions of both strong and weak interaction through the shock wave.

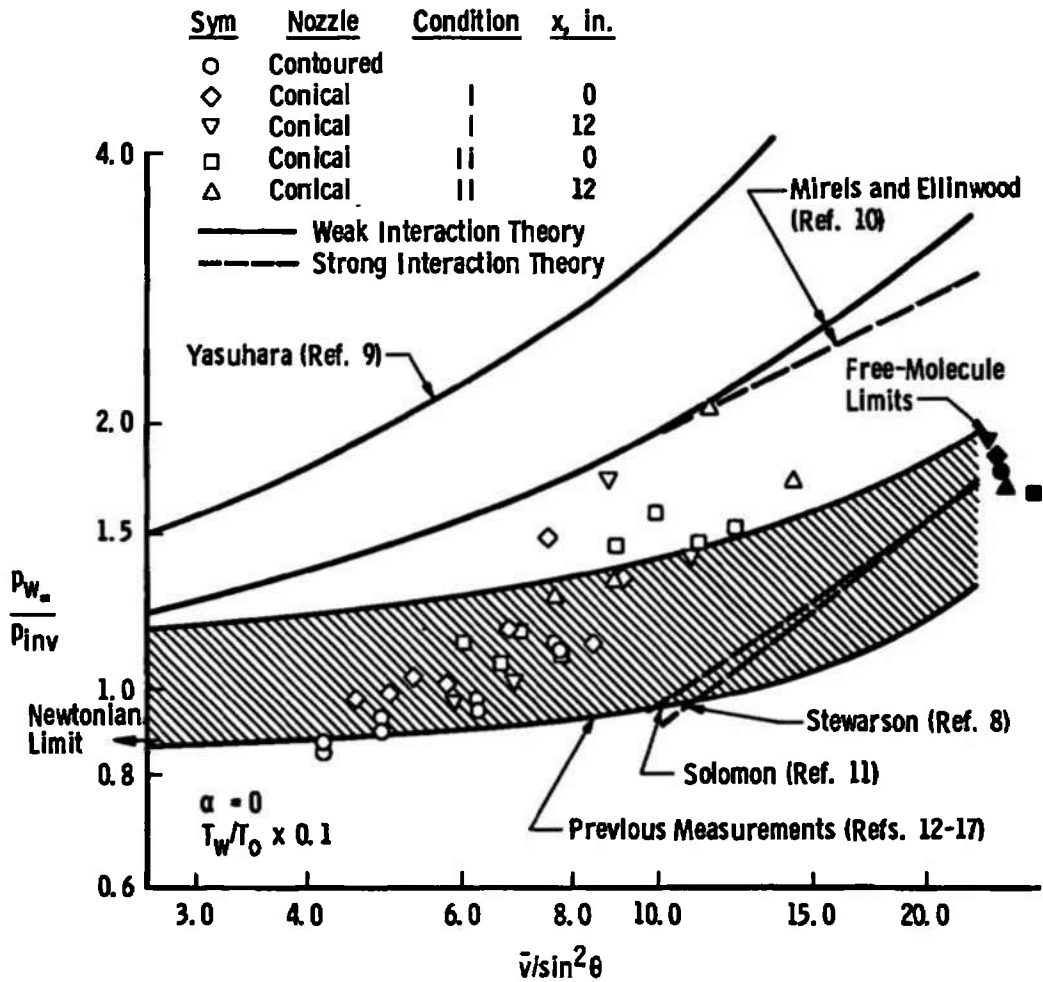


Figure 23. Sharp cone pressure distribution corrected for source flow effects.



A cursory inspection of Fig. 23 reveals that the present corrected results are above previous results at the larger values of  $\bar{v}/\sin \theta$  (low Reynolds number) and appear to be heading above the free-molecule limit. Several statements can be made concerning these observations. In regard to the disagreement between the present and previous results, it should be pointed out that the present data were corrected, as described in Appendix B, taking into account the effect of shear stress and the accommodation of the gas to the cone surface. However, the previous data have been corrected for the orifice effect by the method reported in Ref. 4 which is valid only for complete accommodation of the gas to the surface and for zero shear stress. Under the present conditions the effect of the accommodation coefficient is significant. For example, as stated earlier, the correction used ( $\alpha_e = 0.79$ ) was as much as 100 percent of the measured pressure, whereas for  $\alpha_e = 1.0$  the correction would be only about 60 percent. The effect of shear stress under the present condition is less than the effect of  $\alpha_e$  and of opposite sign; i.e., the pressure correction is decreased by as much as 18 to 20 percent.

Applying these rough estimates to the previous results, it can be shown that at the higher values of  $\bar{v}/\sin^2 \theta$  the band shown on Fig. 23 could be raised by as much as 40 percent, which would then be in agreement with the present results. If the present data were corrected for complete accommodation and zero shear stress, then better agreement with previous results could also be achieved. However, this would represent inaccurate and incomplete corrections. Therefore, the proper procedure would be to correct previous data, taking into account the gas-surface interactions and the shear stress at the model surface. Exact parameters are unknown to the present author and therefore it was not possible to make these corrections to previous results in the present work. In order to illustrate the magnitude of the orifice correction for the present data, Fig. 24 is presented to give the ratio of the uncorrected pressure,  $p_i$ , to the inviscid pressure.

Attention now turns to the free-molecule limits as shown on Fig. 23. The free-molecule pressure is the pressure that would exist at the surface of a cone whose characteristic dimension, e.g., length, is small compared to the gas mean free path. It is generally assumed, or at least implied, that the surface pressure on a sharp cone under all flow conditions should approach the free-molecule limit as one approaches the tip. This is not necessarily the case. Joss and Bogdonoff (Ref. 21) and Videl, et al. (Ref. 22) have shown that even for a sharp flat plate the free stream is disturbed upstream of the leading edge. There is

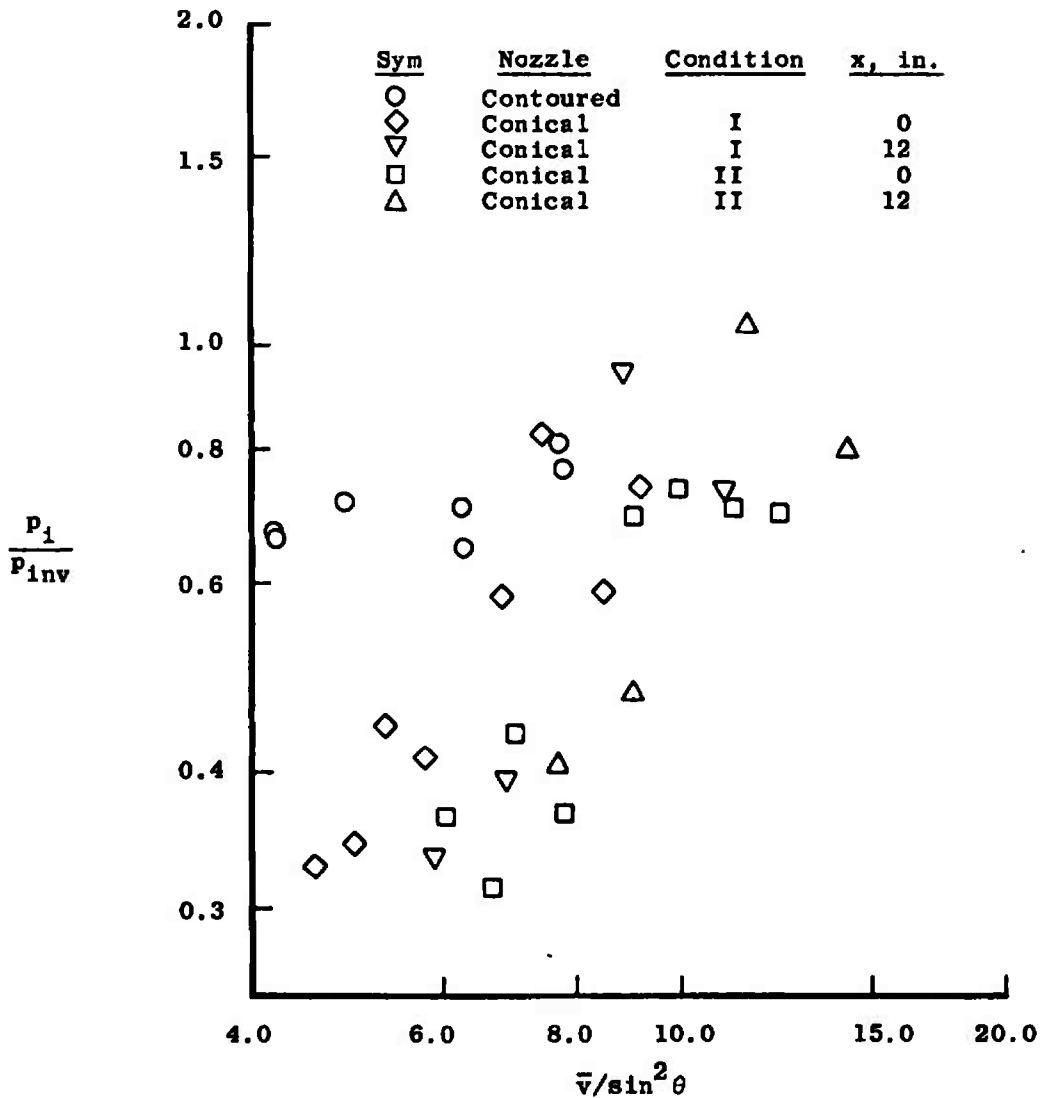


Figure 24. Present data uncorrected for orifice or source flow effects.

even a greater disturbance for the case of a cone since molecules reflected from the cone surface and directed upstream can collide with free-stream molecules and thereby change the free-stream density and velocity approaching the cone. The free-molecule limit is approached at the cone tip only for an infinitely slender cone or needle.

A maximum in the surface pressure has been observed downstream of the leading edge for the case of the cooled flat plate (e.g., Becker, Ref. 23) and the hot wall sharp cone (e.g., Vas, et al., Ref. 14). This

effect has not been observed for the cooled sharp cone, but it may occur closer to the tip. This would cause the data, as shown in Fig. 23, to decrease at larger values of  $\bar{v}/\sin^2 \theta$ .

### 3.4.2 Blunt Cone

Figures 25 through 29 present the results of the tests on the blunt cone with  $C_p$  given as a function of  $\alpha$ . The pressure coefficient is based upon the corrected surface pressure and the conditions at the virtual apex of the conical section of the model. This reference point is the same point relative to the model base as used for the sharp cone. That is, the model was not moved; only the nose section was changed to obtain the blunt cone configuration.

As was done for the sharp cone, the results of the pressure coefficient on the blunt cone are normalized to the value at zero angle of attack with the results shown as bands in Fig. 30. Comparing Fig. 30 with Figs. 19 and 20 reveals that the results for both the sharp and the blunt cones are very similar. It can, therefore, be concluded that for the blunt cone, as was the case for the sharp cone, the effect of source

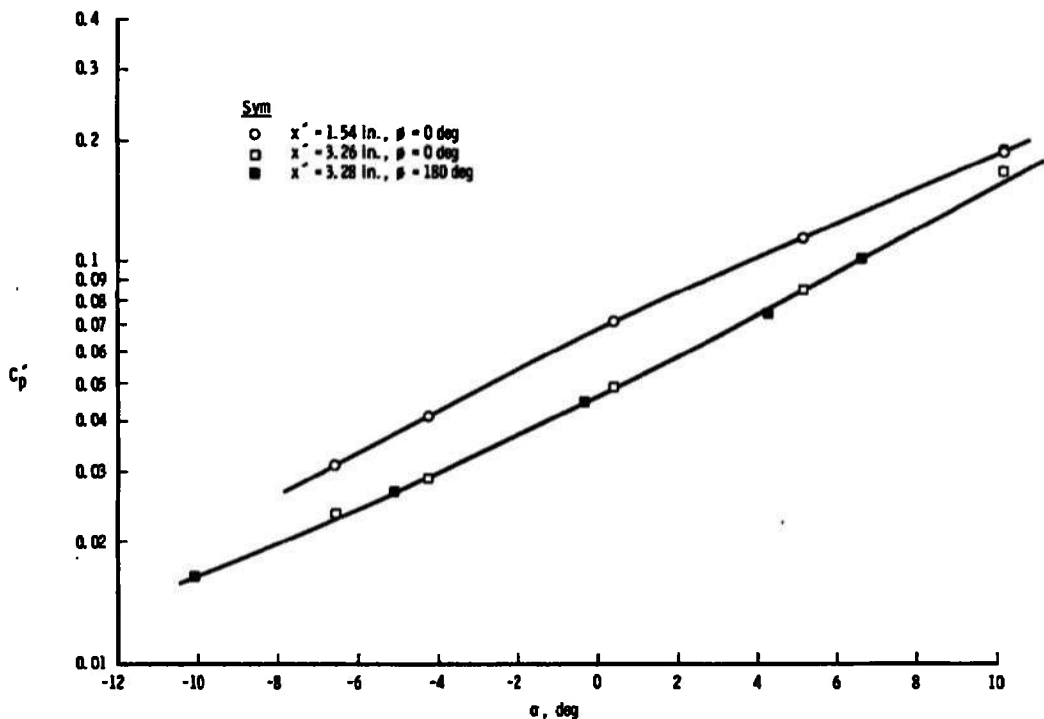


Figure 25. Blunt cone experimental pressure coefficient in the contoured nozzle for  $\phi = 0, 180$  deg.

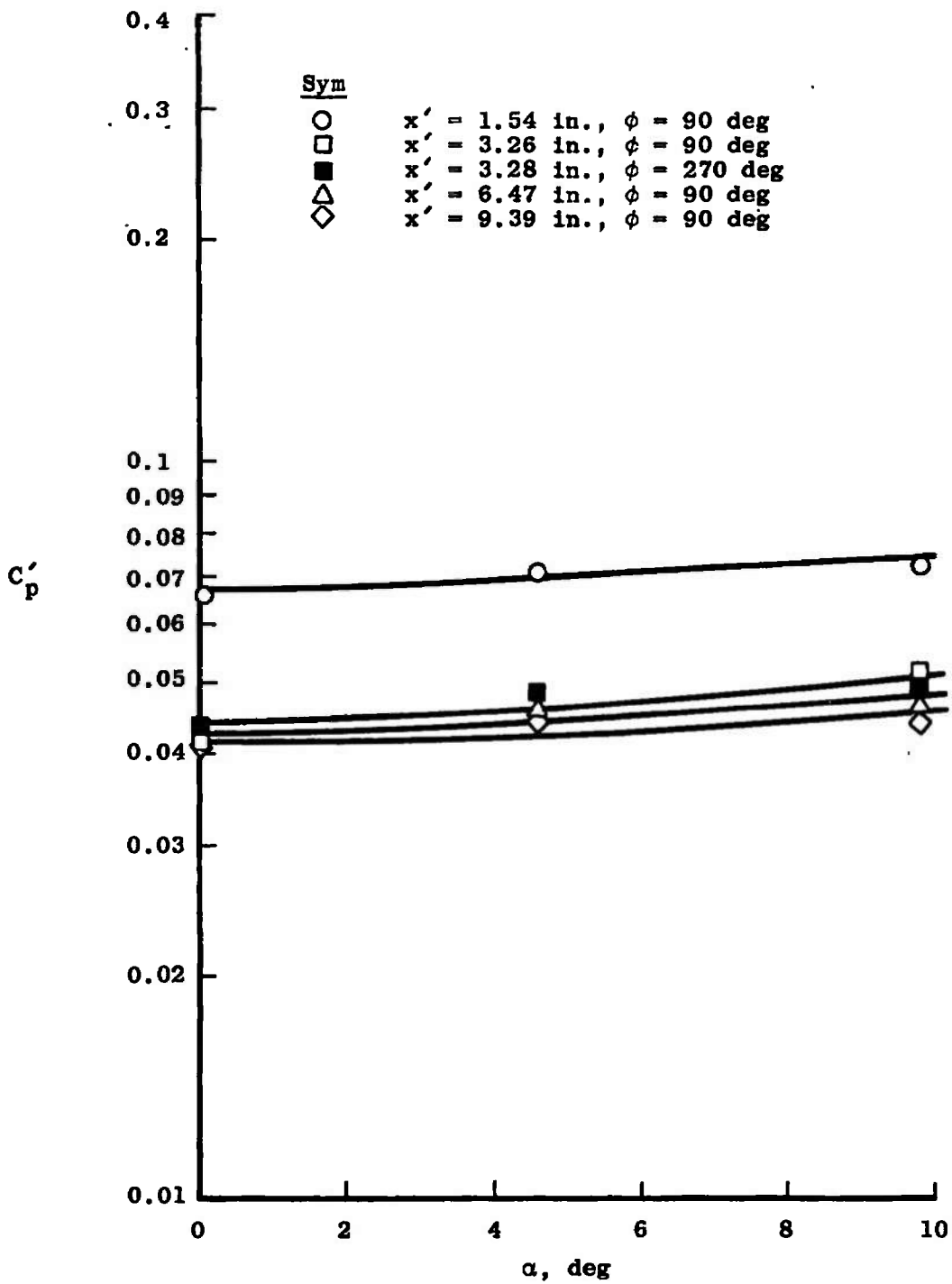


Figure 26. Blunt cone experimental pressure coefficient in the contoured nozzle for  $\phi = 90$  deg,  $270$  deg.

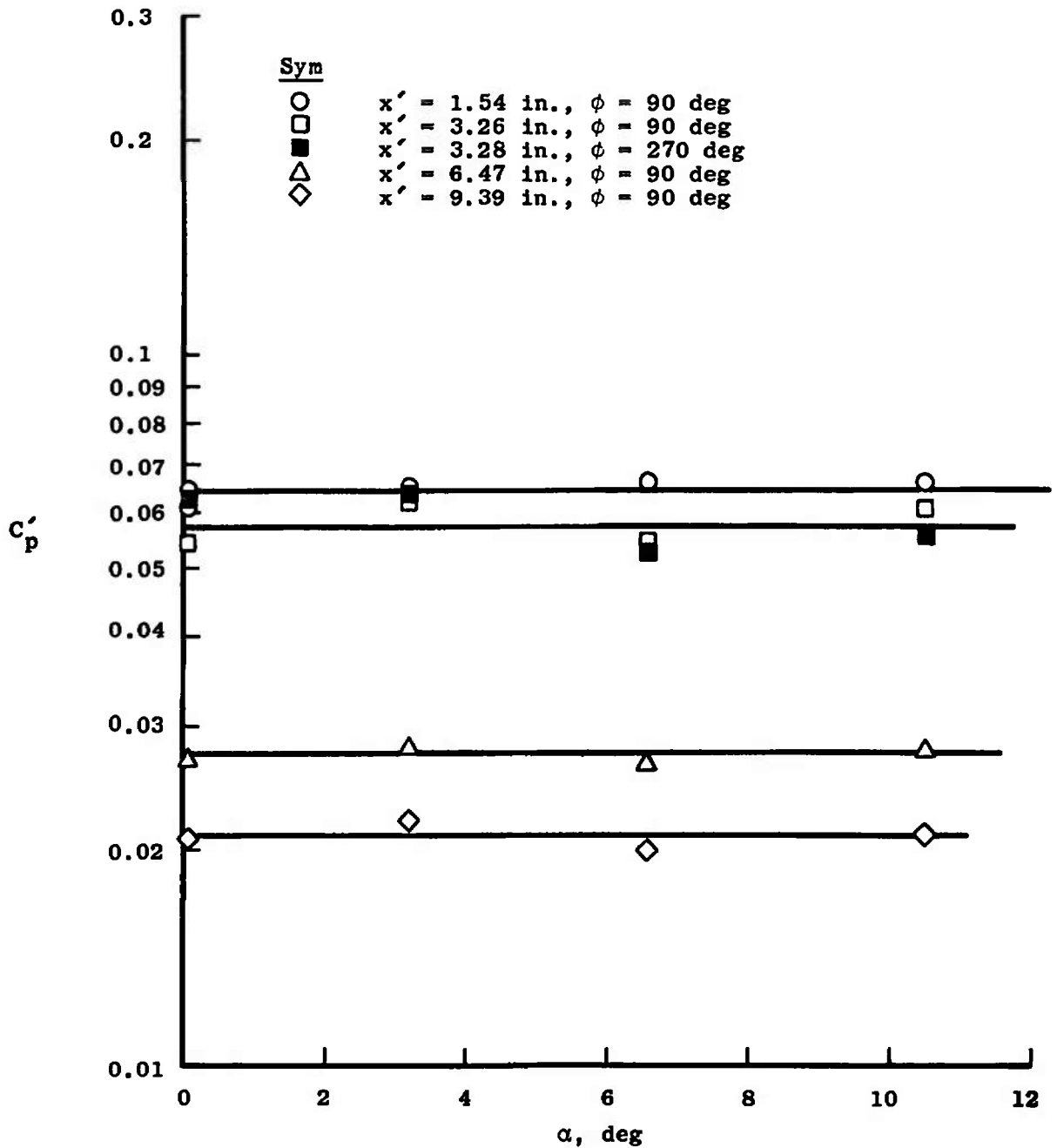


Figure 27. Blunt cone experimental pressure coefficient for Condition I in the conical nozzle for  $x = 0$  and  $\phi = 90$  deg, 270 deg.

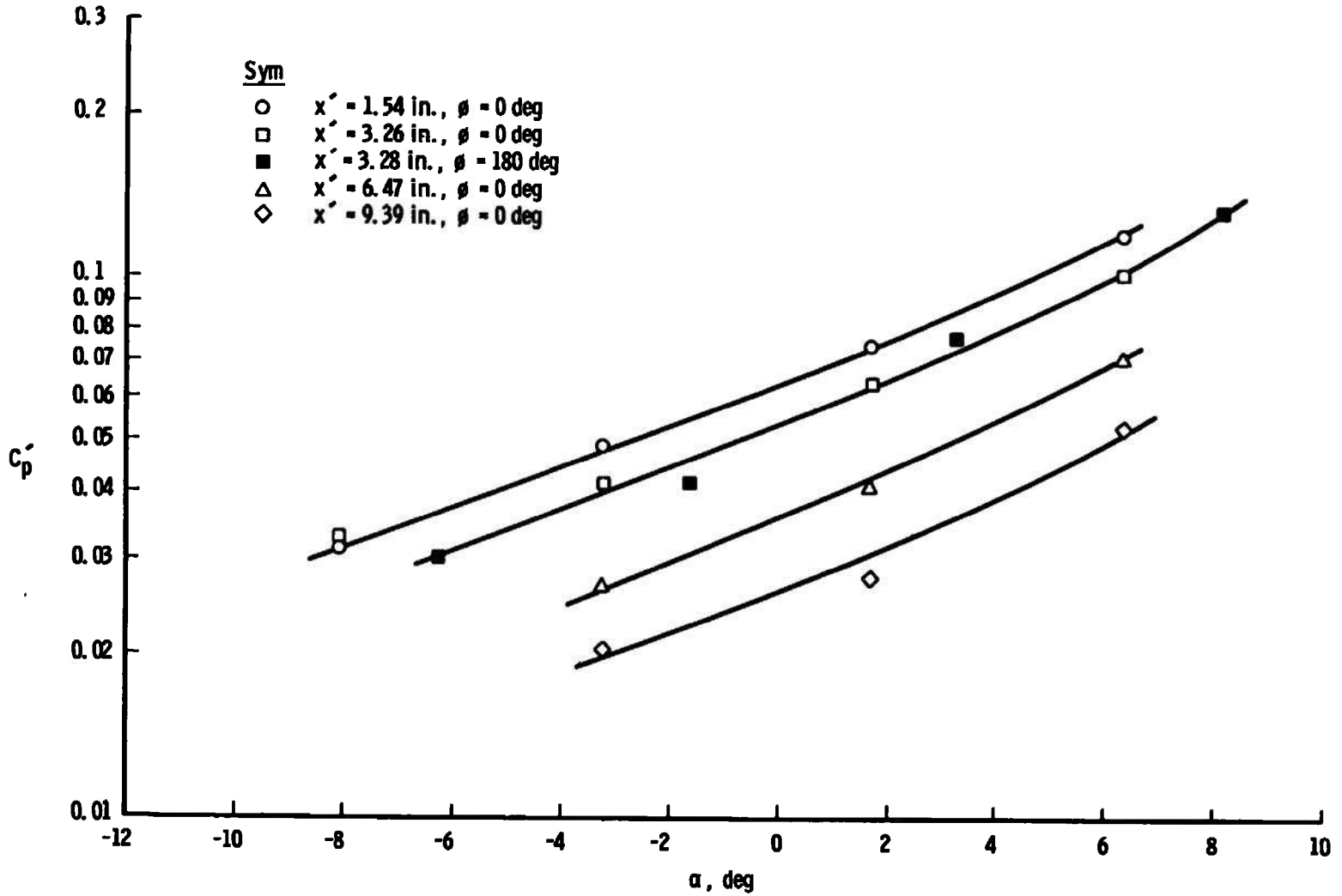


Figure 28. Blunt cone experimental pressure coefficient for Condition II in the conical nozzle for  $x = 0$  and  $\phi = 0, 180$  deg.

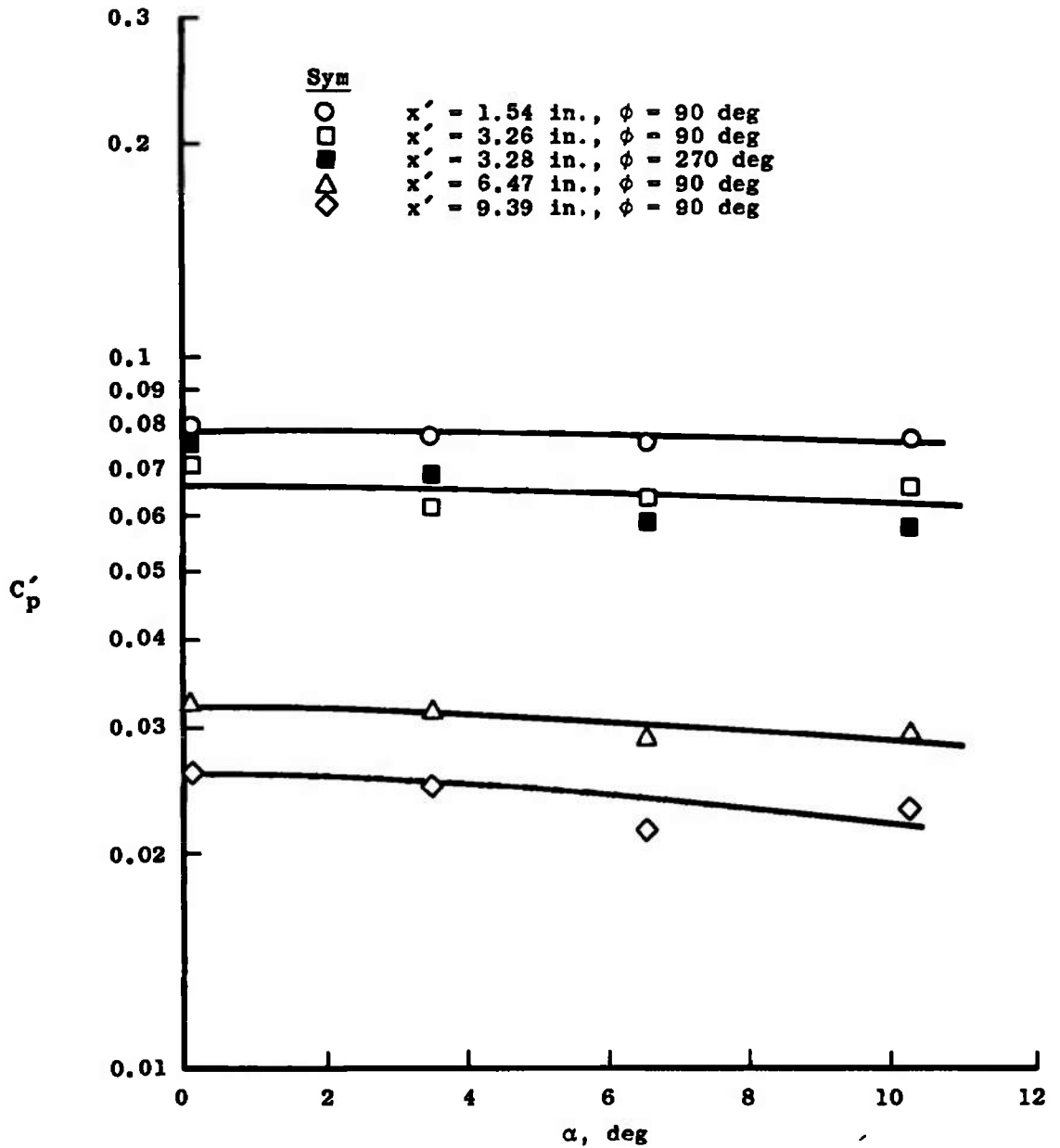


Figure 29. Blunt cone experimental pressure coefficient for Condition II in the conical nozzle for  $x = 0$  and  $\phi = 90$  deg, 270 deg.

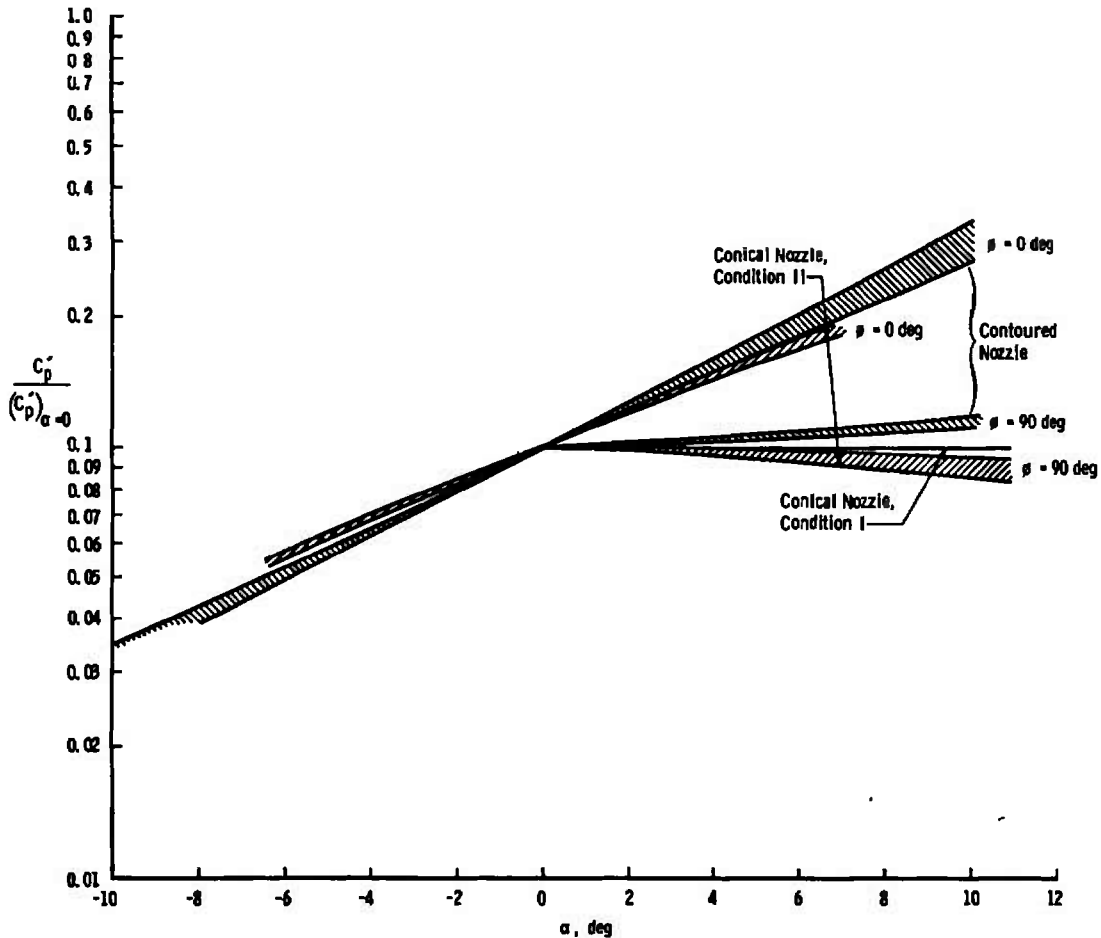


Figure 30. Experimental variation of pressure coefficient ratio with angle of attack for the blunt cone.

flow on the variation of surface pressure with angle of attack is negligible when compared to the variation caused by other parameters such as Reynolds number.

As was true for the sharp cone, almost all previous experimental and theoretical studies of blunted cones have been made for the case of zero angle of attack. One of the best known theories for the pressure distribution on blunted cones under continuous flow conditions is that of Cheng (Ref. 24). Although his theory is not applicable to lower Reynolds number conditions, the correlation parameters suggested by him are widely used.

The present results for  $\alpha = 0$ , obtained by interpolating the data as shown in Figs. 25 through 29, are presented in Fig. 31 as a function of



Cheng's bluntness parameters. Notice that further back on the model (larger  $s$ ), there is a greater discrepancy between the data from the contoured and the conical nozzles. As was done for the sharp cone, the surface pressure coefficient was next corrected according to Fig. 9. It was possible to use the same corrections as for the sharp cone since the virtual apex of the cone was used as the reference point and the Newtonian correction depends upon the model only through the local surface orientation which is the same on the conical portion of both models.

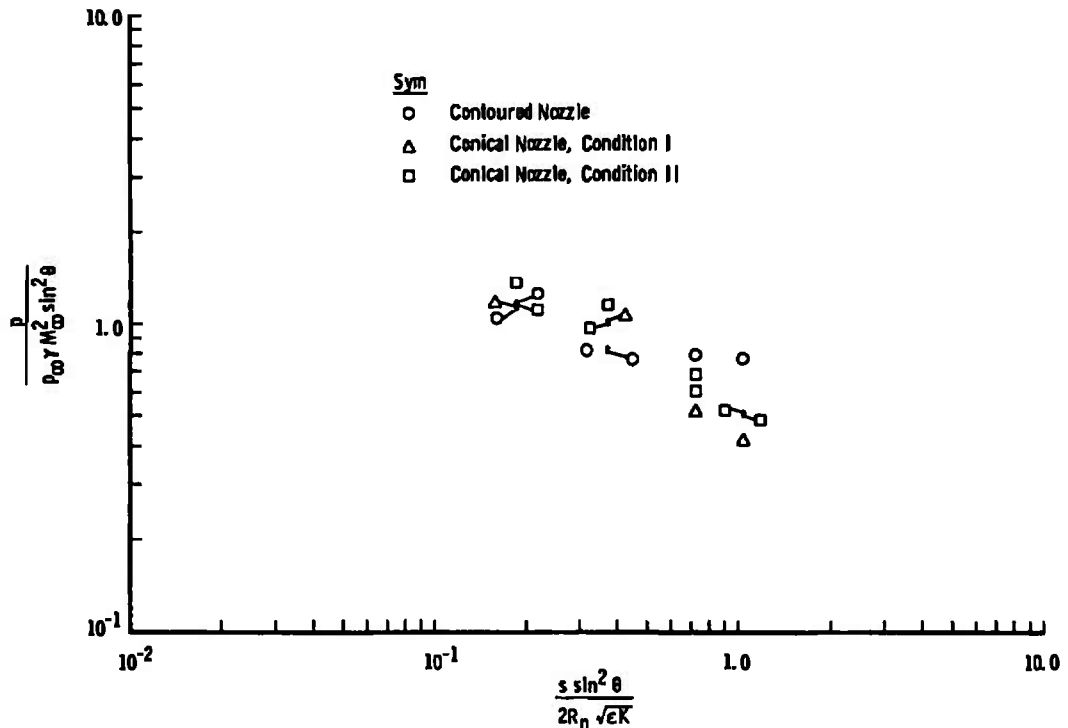


Figure 31. Experimental blunt cone results for  $\alpha = 0$  as a function of Cheng's parameters.

The corrected data are shown in Fig. 32 together with the theory of Cheng and previous experimental data (Refs. 14, 16, 18, and 25 through 28). The scatter of the present data at the higher abscissa values has been reduced by using the Newtonian correction. Notice that none of the experimental results follow the gyrations predicted by Cheng and that the pressure is greater for the lower Reynolds number data. At lower Reynolds number the bluntness is less of an effect because of the thicker boundary layer.

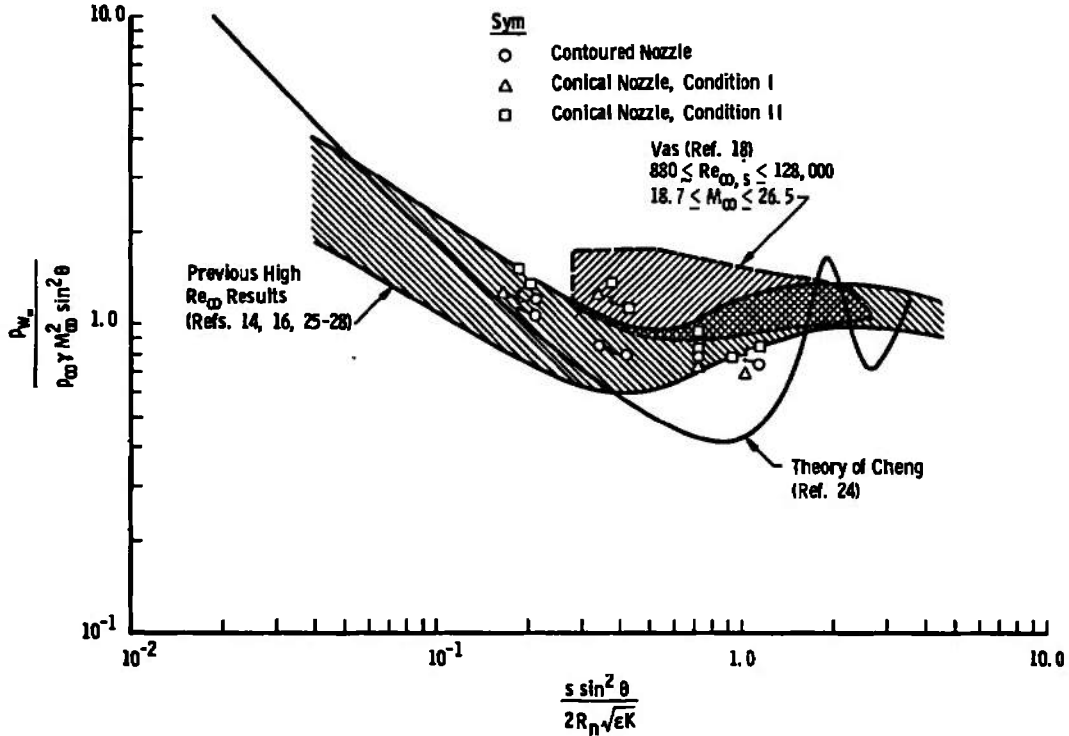


Figure 32. Blunt cone pressure distribution corrected for source flow effects.

In an attempt to better correlate the present results and those of Vas (Ref. 18), the data are plotted as shown in Fig. 33. The ordinate is the same as Cheng's, but the abscissa is a combination of the free-stream Reynolds number based on distance along the surface from the stagnation point and the parameter  $\theta$ ,  $\epsilon$ , and  $K$  from Cheng's other variable. Notice that the scatter has been reduced significantly for both the present data and those of Vas. Comparison of the data of Vas with the present data, which were obtained on a blunter cone, reveals that there is still a bluntness effect, although less than predicted by Cheng.

The comments made earlier in regard to the orifice correction on the sharp cone also would apply to the blunt cone results; i.e., the orifice correction made for the previous measurements does not include the effect of skin friction and nonunity accommodations of the gas to the model surface.

In the transitional regime between high and low Reynolds numbers, it appears that for blunt cones there are no correlation parameters which will reduce the experimental results to a single curve.

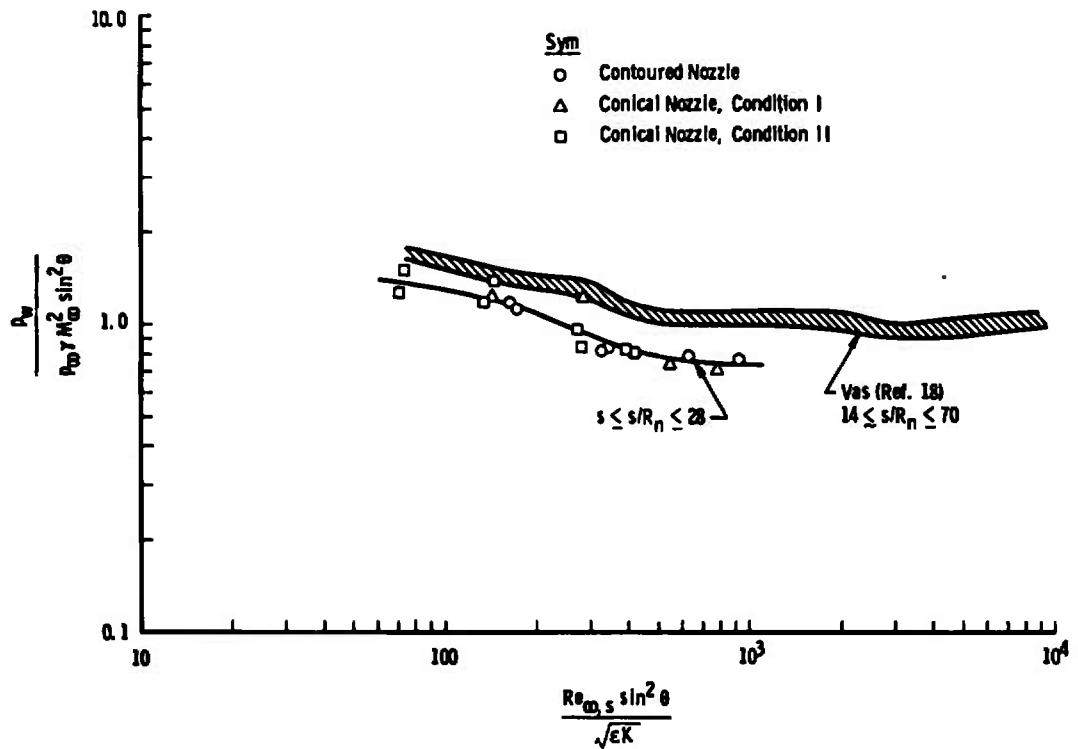


Figure 33. Comparison of present results with those of Vas.

#### 4.0 SUMMARY AND CONCLUDING REMARKS

The results of the present study show that under rarefied flow conditions the pressure distribution on both blunt and sharp 10-deg cones obtained under nonuniform source flow conditions can be brought into agreement with uniform flow results by a correction based upon Newtonian flow. The results of the sharp cone, when corrected for the source flow and orifice effects, approach the inviscid pressure at large distances from the nose. Near the nose, boundary-layer and other rarefied flow effects cause the measured pressure to increase above the inviscid value, and the data seem to be heading above the free-molecule limit as the cone apex is approached. Possible disagreement between the present data and previous results is probably due to an incomplete orifice correction by earlier investigators.

The results for the blunt cone appear to be in quantitative agreement with previous investigations. However, because of the combined

effects of low Reynolds number, Mach number, and cone bluntness, it was not possible to completely correlate the present data with previous results.

The source flow correction was significant for both the sharp and blunt cones, amounting to as much as 80 percent of the uncorrected value. The orifice correction was even larger under some conditions, amounting to as much as 100 percent of the measured pressure.

It can be concluded that pressure data taken under rarefied source flow conditions can be corrected, based upon the Newtonian approximation to yield useful results. However, care must be exercised when the relative angle between the flow and the surface is small, since low-density effects are greatly magnified because of the boundary layer.

When comparisons are made between pressure data of various investigators, it is important that the appropriate orifice corrections be made before conclusions are reached.

#### REFERENCES

1. Kinslow, M., Busby, M. R. and Potter, J. L. "Low-Density Boundary-Layer Modulation by Suction in a Hypersonic Nozzle." AEDC-TR-72-178 (AD754276), January 1973.
2. Boylan, D. E. "Laminar Heat Transfer on Sharp and Blunt Ten-Degree Cones in Conical and Parallel Low-Density Flow." AEDC-TR-73-106 (AD765546), August 1973.
3. Potter, J. L., Arney, G. D., Jr., Carden, W. H., Jr., and Kinslow, M. "Irreversible Flow in Reservoir and Throat Sections of Wind Tunnels with Constricted-Arc Heaters." AGARDograph 84, 379-412, September 1964.
4. Potter, J. Leith, Kinslow, Max, and Boylan, David E. "An Influence of the Orifice on Measured Pressures in Rarefied Flow." Fourth Symposium on Rarefied Gas Dynamics, Vol. 2, Academic Press, New York, 1966, pp. 175-194.
5. Kinslow, Max, and Potter, J. L. "Re-evaluation of Parameters Relative to the Orifice Effect." Presented at the Seventh International Symposium on Rarefied Gas Dynamics, University of Pisa, Pisa, Italy, June 29 through July 3, 1970.

6. Vidal, Robert J., and Bartz, John A. "Surface Measurements on Sharp Flat Plates and Wedges in Low-Density Hypersonic Flow." Cornell Aeronautical Laboratory, Inc., CAL Report No. AF-2041-A-2, February 1968.
7. Kinslow, Max, and Arney, George D., Jr. "Thermo-Molecular Pressure Effects in Tubes and at Orifices." AGARDograph 119, August 1967.
8. Stewartson, K. "Viscous Hypersonic Flow Past a Slender Cone." The Physics of Fluids, Vol. 7, No. 5, pp. 667-675, May 1964.
9. Yasuhara, M. "Axisymmetric Viscous Flow Past Very Slender Bodies of Revolution." Journal of Aerospace Science, Vol. 29, No. 6, June 1962, pp. 667-679, 688.
10. Mirels, H. and Ellinwood, John W. "Hypersonic Viscous Interaction Theory of Slender Axisymmetric Bodies." AIAA 6th Aerospace Sciences Meeting, New York, January 22-24, 1968, AIAA Paper No. 68-1.
11. Solomon, J. M. "Axisymmetric Laminar Boundary Layers with Very Large Transverse Curvature." NOL-TR-66-225, United States Naval Ordnance Laboratory, February 1967.
12. Waldron, H. F. "Viscous Hypersonic Flow Over Pointed Cones at Low Reynolds Numbers." AIAA Journal, Vol. 5, No. 2, February 1967,
13. Lewis, Clark H., Marchand, Ernest O. and Little, Herbert R. "Mass Transfer and First-Order Boundary-Layer Effects on Sharp Cone Drag, Part II: At Hypersonic Conditions." AIAA Journal, Vol. 4, No. 11, November 1966, pp. 1954-1960.
14. Vas, I. E., McDougall, J. G., Koppenwallner, G. and Bogdonoff, S. M. "Some Exploratory Experimental Studies of Hypersonic Low Density Effects on Flat Plates and Cones." Fourth Symposium on Rarefied Gas Dynamics, Vol. 1, edited by J. H. deLeeuw, Academic Press, New York, 1966, pp. 508-534.
15. Burk, A. F. and Douling, E. D. "Aerodynamic Aspects of the Use of a Blunt, Slender Cone as an Air-Data Probe at Hypersonic Speeds." Cornell Aeronautical Laboratory, Inc., CAL Report No. AA-1577-Y4, November 1962.

16. Wilkinson, David B. and Harrington, Shelby A., "Hypersonic Force, Pressure, and Heat Transfer Investigations of Sharp and Blunt Slender Cones." Arnold Engineering Development Center, AEDC-TDR-63-177 (AD414616), August 1963.
17. Glick, H. S., Hofland, R., Jr. and Hollinges, H. B. "Hypersonic Flow Studies." Aerospace Research Laboratories, ARL 69-0079, May 1969.
18. Vas, Irwin E. "An Experimental Study of the Flow About a Slender Cone at Hypersonic Speeds." Ph. D. Dissertation, New York University, May 1970.
19. McCroskey, W. J. "Pressure Distributions on Sharp Cones in Rarefied Hypersonic Flow." AIAA Journal, Vol. 5, No. 11, pp. 2103-2104, November 1967.
20. Sims, Joseph L. "Tables for Supersonic Flow Around Right Circular Cones at Zero Angle of Attack." NASA SP-3004, 1964.
21. Joss, W. W. and Bogdonoff, S. M. "A Detailed Study of the Flow around the Leading Edge of a Flat Plate in Hypersonic Low Density Flow." Sixth Symposium on Rarefied Gas Dynamics, Vol. 1, Academic Press, New York, 1969, pp. 483-492.
22. Vidal, R. J., Merritt, G. E., and Bartz, J. A. "Flowfield Surveys in the Leading Edge Region of a Sharp Flat Plate." Cornell Aeronautical Laboratory, Inc., CAL Report No. AF-2919-A-2, February 1971.
23. Becker, Manfred "Flat Plate Flow Field and Surface Measurements from Merged Layer into Transition Regime." Sixth Symposium on Rarefied Gas Dynamics, Vol. 1, Academic Press, New York, 1969, pp. 515-528.
24. Cheng, H. K. "Hypersonic Flow with Combined Leading-Edge Bluntness and Boundary-Layer Displacement Effect." Cornell Aeronautical Laboratory, Inc., CAL Report No. AF-1285-A-4, August 1960.
25. Little, Herbert R. and Marchand, Ernest O. "Vorticity Influences on Flow Fields of Slender Cones at Hypersonic Speeds." Arnold Engineering Development Center, AEDC-TR-68-263 (AD850520), April 1969.

26. Creel, T. R., Jr., Miller, C. G. III, Maddalon, D. V. and Watson, R. D. "Pressure Distributions and Aerodynamic Characteristics of 9° and 15° Blunted Cones in Nitrogen and Helium at Mach 20." National Aeronautics and Space Administration, NASA Tech. Note, NASA TN D-4314, March 1968.
27. Lewis, C. H. "Pressure Distribution and Shock Shape over Blunted Slender Cones at Mach Numbers from 16 to 19." Arnold Engineering Development Center, AEDC-TN-61-81 (AD261846), August 1961.
28. Knox, Eugene C. and Lewis, Clark H. "A Comparison of Experimental and Theoretically Predicted Pressure Distributions and Force and Stability Coefficients for a Spherically Blunted Cone at  $M_\infty = \sim 18$  and Angles of Attack." Arnold Engineering Development Center, AEDC-TR-65-234 (AD627317), February 1966.

## APPENDIX A CORRECTION OF PITOT PRESSURE FOR ORIFICE AND PROBE EFFECTS

Under rarefied flow conditions impact pressure probes may not indicate the ideal impact pressure because of viscous and transitional flow phenomena. The viscous effects are attributable to the thickening of the boundary layer and shock and their eventual merging. At lower Reynolds numbers the shock becomes more diffuse and the flow departs further from equilibrium as free-molecular conditions are approached. In the present report, all free-molecular conditions are based on equations from Ref. A-1. The specific effects considered are the external or probe effect which was reported by Potter and Bailey (Ref. A-2), and the orifice effect discussed first by Potter, Kinslow, and Boylan (Ref. A-3) for a nonequilibrium state attributable to a flux of energy at a surface. The ideal impact pressure is needed in order to determine conditions in the free stream, so that the measured values must be corrected for the probe and orifice effects.

Various papers have been written on the probe effect. They show that as one proceeds toward more rarefied flow, first a small decrease in the measured impact pressure below the ideal conditions and then an increase in pressures at near-free-molecule conditions are encountered.

The interpretation of impact probe measurements is further complicated by the orifice effect. This effect is manifested by an inequality between the pressure sensed by an orifice and the pressure existing at the surface containing the orifice in the presence of a flux of energy or momentum. The orifice effect was reported in Ref. A-3 for the case of the energy flux to a surface.

The method used to correct pitot probe measurements for the probe and the orifice effect to obtain the true impact pressure follows.

### PROBE EFFECT

A study of impact probes under conditions similar to those in Tunnel M was reported by Daun, et al. (Ref. A-4). An empirical fit to the Daun data and to data from Tunnel M resulted in the following equations for flat-faced probes:

$$\frac{P_w}{P_o} = \frac{\frac{91.4}{(p_w/p_o)_{fm}} + Re_{2,r_p}^2 (\rho_2/\rho_\infty)}{\frac{91.4}{(p_w/p_o)_{fm}^2} + 1.5 Re_{2,r_p} \sqrt{\rho_2/\rho_\infty} + Re_{2,r_p}^2 (\rho_2/\rho_\infty)} \quad (A-1)$$



in which  $p_w$  is the pressure at the face of the probe, obtained from the indicated pressure by applying the orifice correction, and  $p_o'$  is the ideal impact pressure.

The free-molecule limit of  $p_w/p_o'$  for large Mach numbers is

$$\left(\frac{p_w}{p_o'}\right)_{fm} = \left(\frac{2}{\gamma+1}\right)^{\frac{\gamma+1}{\gamma-1}} \frac{\gamma}{\gamma-1} \left(1 + \sqrt{\frac{\pi}{2\gamma} \frac{T_w}{T_\infty} \frac{1}{M_\infty}}\right) \quad (A-2)$$

In order to evaluate these equations an iteration scheme was necessary since  $M_\infty$ ,  $T_\infty$ ,  $Re_{2,r}$ , and  $\rho_2/\rho_\infty$  require the knowledge of  $p_o'$ . The numerical solution is discussed below.

## ORIFICE EFFECT

This effect, attributable to the nonequilibrium state of the gas at the solid boundary, when a flux of energy is present, causes the pressure sensed by an orifice to deviate from the force per unit area on the surface. The amount of deviation is expressed in terms of a dimensionless pressure parameter,  $\bar{p}$ , defined by

$$\bar{p} = \frac{(p_i - p_{ifm})}{(p_w - p_{ifm})} \quad (A-3)$$

where

$p_i$  is the pressure inside the orifice cavity,

$p_{ifm}$  is the true wall pressure in the absence of the orifice

$p_w$  is the true wall pressure in the absence of the orifice.

In Refs. A-3 and A-5,  $\bar{p}$  was shown to be a function of the Knudsen number based on the orifice diameter,  $d$ , the wall temperature,  $T_w$ , and  $p_i$ . However, recent measurements of the orifice effect in Tunnel M and data from Cornell Aeronautical Laboratory (Ref. A-6) show that the results of the correlation parameter used in Refs. A-3 and A-5 are inadequate for higher enthalpy flows. The method of correcting for the orifice effect in this test is based upon a paper presented at the Seventh International Symposium on Rarefied Gas Dynamics at Pisa, Italy, June 30, 1970 (Ref. A-7). The basic material in that paper is given in Appendix B.

The relation between  $\bar{p}$  and a Knudsen number,  $\tilde{K}_n$ , based upon orifice diameter,  $p_w$ , and a reference temperature,  $T_r$ , that was used is

$$\bar{p} = 1.36Z - 0.36Z^2 \quad (A-4)$$

in which

$$Z = (200\tilde{K}_n^2 \gamma w^{-1/4} + 1)^{1/4}$$

where  $w$  is the gas molecular weight.  $p_{ifm}$  and  $T_r$  are both functions of  $K$ , the dimensionless heat-transfer rate parameter, and  $\alpha_e$ , the thermal accommodation coefficient. Definitions of  $p_{ifm}/p_w$  and  $T_r/T_w$  are given by

$$\frac{p_{ifm}}{p_w} = \frac{\sqrt{2\pi} \left( \frac{2 - \alpha_e}{\alpha_e} \right) \kappa + \sqrt{\frac{8\pi\kappa^2(1 - \alpha_e)}{\alpha_e^2} + 4}}{2 - \pi\kappa^2} \quad (A-5)$$

and

$$\frac{T_r}{T_w} = 1 + 2\pi\kappa^2 \left( \frac{2 - \alpha_e}{\alpha_e} \right) - \frac{2\kappa}{\alpha_e^2} \sqrt{2\pi[2\pi\kappa^2(1 - \alpha_e) + \alpha_e^2]} \quad (A-6)$$

where

$$\kappa = \frac{\dot{q}(\gamma - 1)}{p_w(\gamma + 1)\sqrt{RT_w}} \quad (A-7)$$

An iteration scheme is required to solve for  $p_w$ . The thermal accommodation coefficient,  $\alpha_e$ , was presumed to be 0.79 for  $N_2$ .

Based on limited heat-transfer data from Tunnel M for flat-faced bodies, the following equation was used to calculate the stagnation point heat transfer:

$$\dot{q} = \frac{\dot{q}_{fm}}{\left[ \left( \frac{\dot{q}_{fm}}{\dot{q}_{FR}} \right)^5 + 1 \right]^{1/5}} \quad (A-8)$$

where  $\dot{q}_{fm}$  is the free-molecule heat-transfer rate and  $\dot{q}_{FR}$  is from the continuum Fay-Riddell equation (Ref. A-9). This expression gives the correct free-molecule heat-transfer rate and approaches the Fay-Riddell theory for higher Reynolds numbers.

The equations used for  $\dot{q}_{fm}$  and  $\dot{q}_{FR}$  for higher Mach numbers are

$$\dot{q}_{fm} = -\alpha_e p_\infty \sqrt{RT_\infty} \left\{ \left[ \frac{\gamma}{2} M_\infty^2 + \frac{\gamma}{\gamma-1} - \frac{(\gamma+1)}{2(\gamma-1)} \frac{T_w}{T_\infty} \right] \sqrt{2\pi\gamma} M_\infty \right\} \quad (A-9)$$

and based upon Ref. A-9, the heat-transfer rate to a flat-faced probe of radius  $r$  is

$$\dot{q}_{FR} = -0.54 \sqrt{2} \left( \frac{T_o}{T_w} \frac{\mu_w}{\mu_o} \right)^{0.1} \sqrt{\frac{\mu_o p_o'}{RT_o}} \sqrt{\frac{4U_\infty}{3\pi r_p}} \sqrt{2 \frac{\rho_\infty}{\rho_2} \left( 1 - \frac{1}{2} \frac{\rho_\infty}{\rho_2} \right) \left( \frac{h_o - h_w}{(P_r)^{0.6}} \right)} \quad (A-10)$$

based upon the results of Ref. A-9. Heat-transfer rate is negative for "cold wall" conditions.

If free-stream properties are known, then Eqs. (A-1) through (A-10) can be solved to permit the correction of data for the orifice and probe effects. However, since free-stream conditions are known only after applying the correction, an iteration scheme was used. The numerical method for correcting the pitot data is described briefly below.

### ITERATION PROCEDURE

An iteration procedure was used to obtain the ideal impact pressure,  $p_o'$ , from the indicated pressure,  $p_i$ . An initial approximation was made equating  $p_o'$  to  $p_i$ . Using the reservoir stagnation pressure, flow properties, such as  $Re_{2,r}$ ,  $\rho_2/\rho_\infty$ ,  $M_\infty$ ,  $T_\infty$ ,  $p_\infty$ , and  $U_\infty$  were obtained using isentropic flow equations along with the value of  $p_o'$ . The stagnation point heat transfer was obtained using Eqs. (A-8), (A-9), and (A-10). The  $p_w$  was assumed equal to  $p_i$ , thereby permitting the solution of  $K$  from Eq. (A-7). Equations (A-3) through (A-6) were solved for  $\bar{p}$  yielding  $p_w$  which was substituted in Eq. (A-7) giving a new  $K$ . Equations (A-3) through (A-6) were repeatedly solved until  $p_w$  did not change from one iteration to the next. Using the obtained value of  $p_w$  in Eqs. (A-1) and (A-2),  $p_o'$  was obtained and used to repeat the above procedures until the value of  $p_o'$  was constant for successive iterations. The final value of  $p_o'$  is the ideal impact pressure which can be used to obtain the corrected free-stream properties.

## APPENDIX A REFERENCES

- A-1. Schaaf, S. A. and Chambre, P. L. "Flow of Rarefied Gases." Fundamentals of Gas Dynamics, Section H, edited by Howard Wilson Emmons, Princeton University Press, Princeton, N. J., pp. 687-739.
- A-2. Potter, J. Leith, and Bailey, Allan B. "Pressures in the Stagnation Regions of Blunt Bodies in the Viscous-Layer to Merged-Layer Regimes of Rarefied Flow." ARO Preprint 63-436, Presented at the AIAA Conference on Physics of Entry into Planetary Atmospheres, Massachusetts Institute of Technology, August 1963.
- A-3. Potter, J. Leith, Kinslow, Max, and Boylan, David E. "An Influence of the Orifice on Measured Pressures in Rarefied Flow." Fourth Symposium on Rarefied Gas Dynamics, edited by J. H. deLeeuw, Vol. 2, Suppl. 3, Academic Press, New York, 1966, pp. 175-194. See also AEDC-TDR-64-175 (AD447734).
- A-4. Daum, Fred L., Shang, J. S., and Elliot, Capt. G. A. "Rarefaction Effects on Impact Pressure Probes in Hypersonic Flow." ARL-65-176, September 1965.
- A-5. Kinslow, Max, and Arney, George D., Jr. "Thermo-Molecular Pressure Effects in Tubes and at Orifices." AGARDograph 119, August 1967.
- A-6. Bartz, John A., and Vidal, Robert J. "Experimental Study of Pseudo Transpiration at an Orifice in Rarefied Flow." CAL No. AF-2041-A-3, September 1968. See also Sixth International Symposium on Rarefied Gas Dynamics, Massachusetts Institute of Technology, July 1968, pp. 639-653.
- A-7. Kinslow, Max, and Potter, J. Leith. "Reevaluation of Parameters Relative to the Orifice Effect." Presented at the Seventh International Symposium on Rarefied Gas Dynamics University of Pisa, Pisa, Italy, June 29 through July 3, 1970.
- A-8. Teagan, William P. and Springer, George S. "Heat Transfer and Density-Distribution Measurements between Parallel Plates in the Transition Regime." The Physics of Fluids, Vol. 11, No. 3, March 1968, p. 497-506.

- A-9. Fay, J. A. and Riddell, F. R. "Theory of Stagnation Point Heat Transfer in Dissociated Air." Journal of Aeronautical Sciences, Vol. 25, No. 2, February 1958, pp. 73-85, 121.

## APPENDIX B REEVALUATION OF PARAMETERS RELATIVE TO THE ORIFICE EFFECT

Max Kinslow and J. Leith Potter

Note: The material contained in this Appendix was presented at the Seventh International Symposium on Rarefied Gas Dynamics which met in 1970 at Pisa, Italy. J. Leith Potter was a co-author of this work. Since at the present (September 1973) the proceedings of this conference have not been published, it was decided to include the basic material of that presentation as part of this report so as to make it available to the reader.

### INTRODUCTION

At the Fourth International Symposium on Rarefied Gas Dynamics, the present authors and a colleague first discussed the problem of estimating corrections to pressures measured within cavities in surfaces when a condition of energy exchange such as aerodynamic shear and/or heat transfer exists at the surface. (Ref. B-1). It was shown theoretically and confirmed experimentally that finite energy transfer of this type causes pressures,  $p_i$ , measured within cavities to be different, in general, from the desired force per unit area,  $p_w$ , on the surface at the cavity orifice. This phenomenon was analyzed on the basis that the aerodynamic shear could be neglected so long as the shear stress is not comparable to the local pressure. An expression for the pressure in the cavity was derived for the case where orifice diameter,  $d$ , is much less than a local mean-free path,  $\lambda$ . Experimental data were presented for the transitional flow regime, and the combined theory and experiment enabled the construction of a semiempirical method for correcting measured pressures to account for the "orifice effect" when finite heat-transfer rates existed.

In 1967, Kinslow and Arney (Ref. B-2) extended the experimental investigation by collecting and analyzing a large number of new, direct measurements of orifice effect. They also discussed and gave data on the role of thermal accommodation coefficient in this problem. This reference, along with a later paper, also contains much useful information on thermo-molecular pressure effects in tubes (Ref. B-3).

When applied to the data on effect of varying orifice diameter in rarefied flows available prior to 1968, this earlier method seemed quite satisfactory. In the earlier analysis the authors had chosen to use wall temperature,  $T_w$ , as a characteristic temperature in calculating and correlating orifice effect. However, in the light of some recent experiments, it was concluded that gas temperatures external to the orifice should have a more prominent role in correlating the data. At this time, the authors present a reevaluation of the orifice effect phenomenon starting on the basis of the first paper (Ref. B-1) but now including consideration of shear stress and using a correlating parameter for the transitional flow regime which is based on gas temperatures adjacent to the orifice. The free-molecular case is reviewed first to define terms and to establish the limiting (maximum) "orifice" correction. This is followed by presentation of the results of correlating transitional flow data and the steps involved in application of the correction are outlined.

## ANALYSIS

A two-sided Maxwellian velocity distribution is utilized where a minus superscript denotes incoming molecules with negative components of velocity normal to the solid surface and a plus superscript applies to outgoing molecules with positive normal components of velocity. Diffuse reflection of molecules from the solid surface is assumed, and the following velocity distribution functions are used:

$$f^- = \frac{n^-}{(2\pi RT^-)^{3/2}} \exp \left[ -\frac{(\xi_x - U_x)^2 + \xi_y^2 + \xi_z^2}{2RT^-} \right] \quad (B-1)$$

and

$$f^+ = \frac{n^+}{(2\pi RT^+)^{3/2}} \exp \left( -\frac{\xi_x^2 + \xi_y^2 + \xi_z^2}{2RT^+} \right) \quad (B-2)$$

where

- |   |                    |
|---|--------------------|
| $n$ = molecular number density                                      | $R$ = gas constant |
| $\xi$ = molecular velocity  | $T$ = temperature  |
| $x, y, z$ = Cartesian coordinates                                   |                    |
| $U_x$ = average tangential velocity component of incoming molecules |                    |

It is assumed that the corresponding normal component of velocity is zero at the surface. From Eqs. B-1 and B-2, surface pressure and shear stress are, respectively,

$$p_w = mn^-(RT^-/2)[1 + (T^+/T^-)^{1/2}] \quad (\text{B-3})$$

and

$$\tau = mn^-U_x(RT^-/2\pi)^{1/2} \quad (\text{B-4})$$

where  $m$  is the molecular mass.

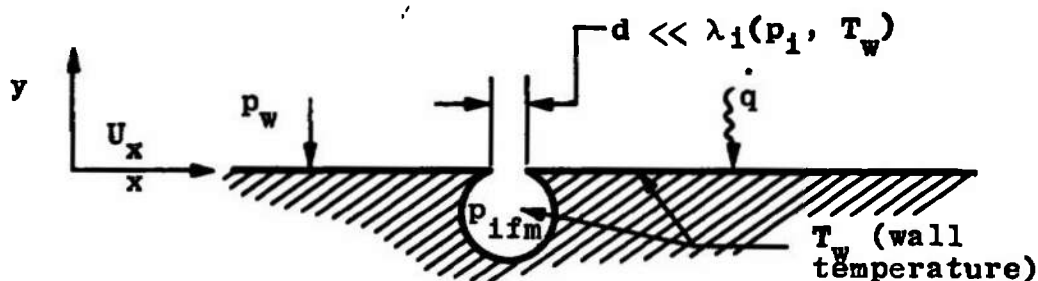
The number of molecules incident per unit area and time, is

$$N^- = n^-(RT^-/2\pi)^{1/2} \quad (\text{B-5})$$

Correspondingly, for outgoing molecules,

$$N^+ = n^+(RT^+/2\pi)^{1/2} \quad (\text{B-6})$$

For the orifice cavity in a surface as sketched below,



the steady-state net flux of molecules passing through the entrance is zero. The number flux leaving the orifice is, for free-molecular flow,

$$N_{out} = (p_{ifm}/m)(2\pi RT_w)^{-1/2} \quad (\text{B-7})$$

Setting  $N_{out} = N^-$  and solving for the pressure within the cavity,  $p_{ifm}$ , under conditions of  $d \ll \lambda_i$ , the result is

$$p_{ifm} = mn^-RT^-(T_w/T^-)^{1/2} \quad (\text{B-8})$$



The incident-energy, assuming internal and translational energies in equilibrium, is

$$E_i = mn^-RT^- \left( \frac{RT^-}{2\pi} \right)^{1/2} \left( \frac{U_x^2}{2RT^-} + \frac{\gamma+1}{2(\gamma-1)} \right) \quad (B-9)$$

where  $\gamma$  = ratio of specific heats of gas.

Noting that  $N^- = N^+$ , the reemitted energy may be expressed as

$$E_r = mn^-RT^+ \left( \frac{RT^-}{2\pi} \right)^{1/2} \frac{\gamma+1}{2(\gamma-1)} \quad (B-10)$$

Now an energy accommodation coefficient is defined as

$$a_e = (E_i - E_r)/(E_i - E_w) \quad (B-11)$$

where

$$E_w = mn^-RT_w \left( \frac{RT^-}{2\pi} \right)^{1/2} \frac{\gamma+1}{2(\gamma-1)} \quad (B-12)$$

The heat-transfer rate, negative when from gas to surface, is

$$\dot{q} = E_r - E_i = -a_e(E_i - E_w) \quad (B-13)$$

The foregoing equations have been solved analytically, making it possible to compute  $p_{ifm}/p_w$  as a function of  $a_e$ ,  $\dot{q}$ ,  $\tau$ ,  $T_w$  and the gas properties when  $d \ll \lambda_j$ . The analytical result is cumbersome, and to save space it is not given. Figure B-1 presents the solution graphically; the parameters are defined as

$$\zeta = (\tau/p_w)(\pi/2)^{1/2} [(\gamma-1)/(\gamma+1)]^{1/2} \quad (B-14)$$

$$\kappa = \dot{q}(\gamma-1)/[p_w(\gamma+1)(RT_w)^{1/2}] \quad (B-15)$$

A simple empirical expression that fits Fig. B-1 essentially exactly is

$$\left( \frac{p_{ifm}}{p_w} \right)^2 \frac{\left( \frac{\pi}{2} \kappa^2 - 1 \right)}{(1 + \zeta^2)^2} + \left( \frac{p_{ifm}}{p_w} \right) \frac{(2\pi)^{1/2} \kappa \left( \frac{2 - a_e}{a_e} + \zeta^2 \right)}{(1 + \zeta^2)^2} + 1 = 0 \quad (B-16)$$

## CORRELATION OF EXPERIMENTAL DATA

The data for each particular gas in Refs. B-1 and B-2 were found to correlate with a Knudsen number,  $\tilde{K}_n = \lambda(p_i, T_r)/d$ , based on pressure in the cavity,  $p_i$ , a reference temperature,  $T_r$ , and orifice diameter,  $d$ , where, with  $T_o^- = T^- + U_x^2(\gamma-1)/(\gamma R)$

$$T_r = (T_o^- + T^+)/2 \quad (\text{B-17})$$

Unfortunately the analytic solution of Eq. (B-17) is even more awkward than the result for  $p_{ifm}/p_w$ . Therefore a graphical and curve fitting approach again is chosen for presentation. Within the limits  $p_{ifm}/p_w \leq 1$  and  $T_r/T_w \lesssim 20$ , which encompass all the experimental data known to us (Refs. B-1, B-2, B-4, and B-5) we find that the reference temperature ratio may be represented empirically by

$$T_r/T_w = \left(1 + \frac{\gamma+1}{\gamma} \zeta^2 + \xi \zeta^4\right) (p_{ifm}/p_w)^{-\eta} \quad (\text{B-18})$$

With  $p_{ifm}/p_w$  from Fig. B-1, Fig. B-2 gives the remaining parameters in Eq. (B-18) as functions of  $\alpha_e$  and  $\xi$ .

Prior to this point the discussion has been based on free-molecule flow, i. e.,  $d \ll \lambda_i$ . To correlate the data of Refs. B-1 and B-2 and facilitate the prediction of orifice effects in the transitional flow regime, it is convenient to introduce the two additional parameters,

$$\bar{p} = [(p_i/p_w) - p_{ifm}/p_w]/(1 - p_{ifm}/p_w) \quad (\text{B-19})$$

and, with  $w$  = gas molecular weight,

$$Z = (200 K_n^2 \gamma w^{-1/4} + 1)^{-1/4} \quad (\text{B-20})$$

Then all the data from the bell jar experiments are satisfactorily represented by a single curve given by the empirical equation

$$\bar{p} = 1.36 Z - 0.36 Z^2 \quad (\text{B-21})$$

## CONCLUDING REMARKS

To apply this method it is necessary to determine  $\gamma$ ,  $R$ ,  $w$ ,  $T_w$ ,  $p_i$ ,  $\dot{q}$ ,  $\tau$ ,  $d$ , and  $\alpha_e$ . Then an iterative procedure is followed wherein a trial value of  $p_w$  is estimated, leading to  $\zeta$  (Eq. B-14) and (Eq. B-15). Thereafter Fig. B-1 yields  $p_{ifm}/p_w$ , Fig. B-2 gives  $\xi$  and  $\eta$ , and Eq. (B-18) is solved for  $T_r/T_w$ . Next  $Kn = \lambda(p_i, T_r)/d$  is calculated and Eqs. (B-20 and B-21) are solved for  $Z$  and  $\bar{p}$ , respectively. From the latter and Eq. (B-19) an improved value of  $p_w$  is obtained. If this differs significantly from the trial value, the steps are repeated. Perhaps it should be pointed out that if the free-stream flow properties were based on the measured pressure being corrected, one must return to these flow conditions to begin the iteration again.

The assumption of values of  $\alpha_e$  obviously has to be accepted in applying the present method to data which typically do not include any measure of that parameter. For air,  $\alpha_e = 0.8$  has been used; for nitrogen,  $\alpha_e = 0.79$ ; and for argon  $\alpha_e = 0.83$ . The values for nitrogen and argon are identical to the thermal accommodation coefficients found by Kinslow and Arney (Ref. B-2); the slightly greater value for air is insignificant practically but follows from consideration of molecular weights of air and nitrogen.

## APPENDIX B REFERENCES

- B-1. Potter, J. Leith, Kinslow, Max, and Boylan, D. E. "An Influence of the Orifice on Measured Pressures on Rarefied Flow." Fourth Symposium on Rarefied Gas Dynamics, edited by J. H. deLeeuw, Vol. 2, Suppl. 3, Academic Press, New York, 1966, pp. 175-194.
- B-2. Kinslow, Max and Arney, George D., Jr. "Thermo-Molecular Pressure Effects in Tubes and at Orifices." AGARDograph 119, August 1967.
- B-3. Kinslow, Max and Arney, George D., Jr. "Corrections for Thermo-Molecular Pressures in Tubes and at Orifices." Sixth Symposium on Rarefied Gas Dynamics, Vol. 1. Academic Press, New York, 1969, pp. 691-698.

- B-4. Guy, R. W. and Winebarger, R. M. "Effect of Orifice Size and Heat-Transfer Rate on Measured Pressures in a Low-Density Arc-Heated Wind Tunnel." NASA TN D-3829, February 1967.
- B-5. Bartz, John A. and Vidal, Robert J. Sixth Symposium on Rarefied Gas Dynamics, Vol. 1. Academic Press, New York, 1969, pp. 639-653. See also "Experimental Study of Pseudo Transpiration at an Orifice in Rarefied Flow," CAL No. AF-2041-A-3, September 1968.

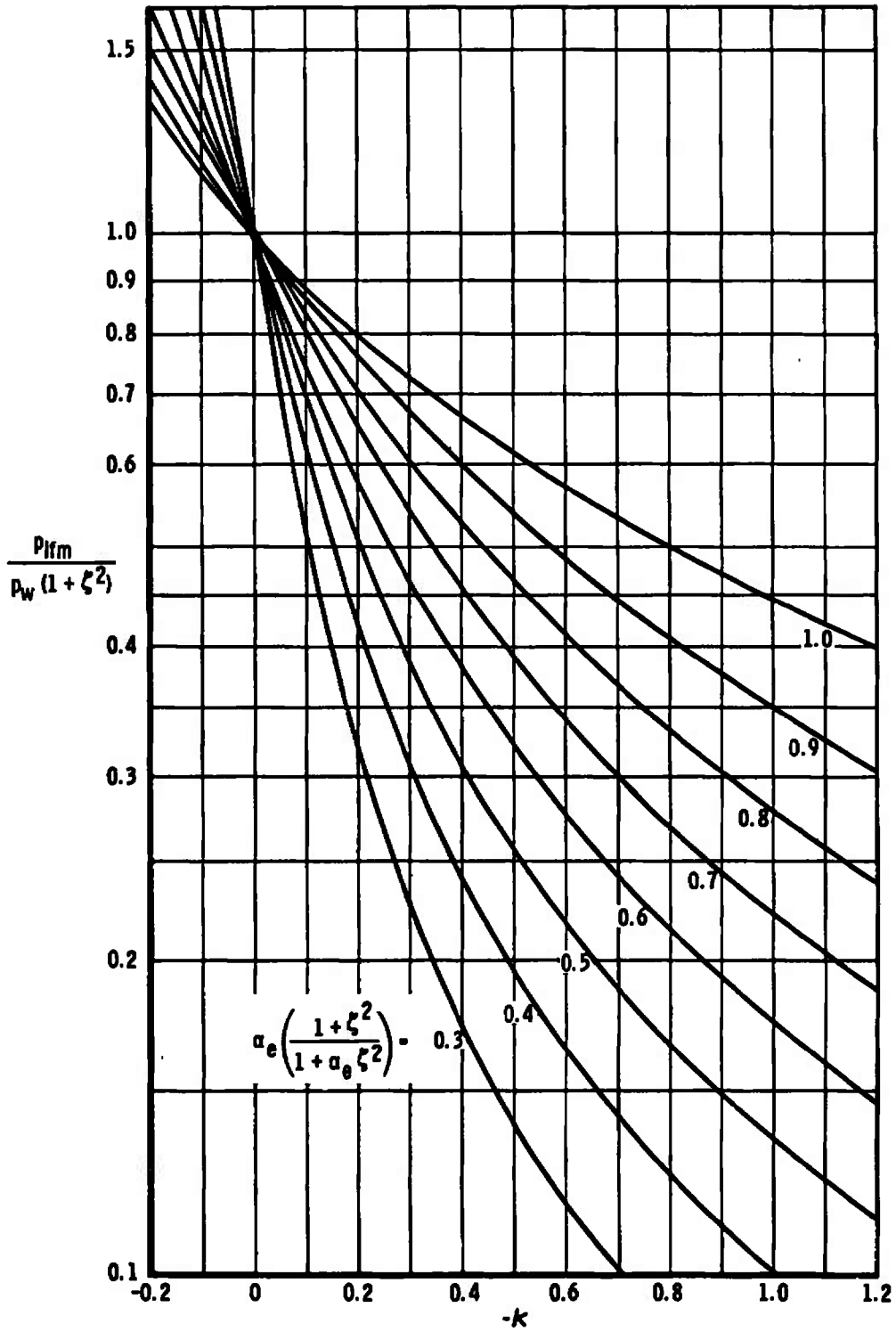


Figure B-1. Solution for  $P_{ifm}/P_w$  with Free-Molecular Flow. .

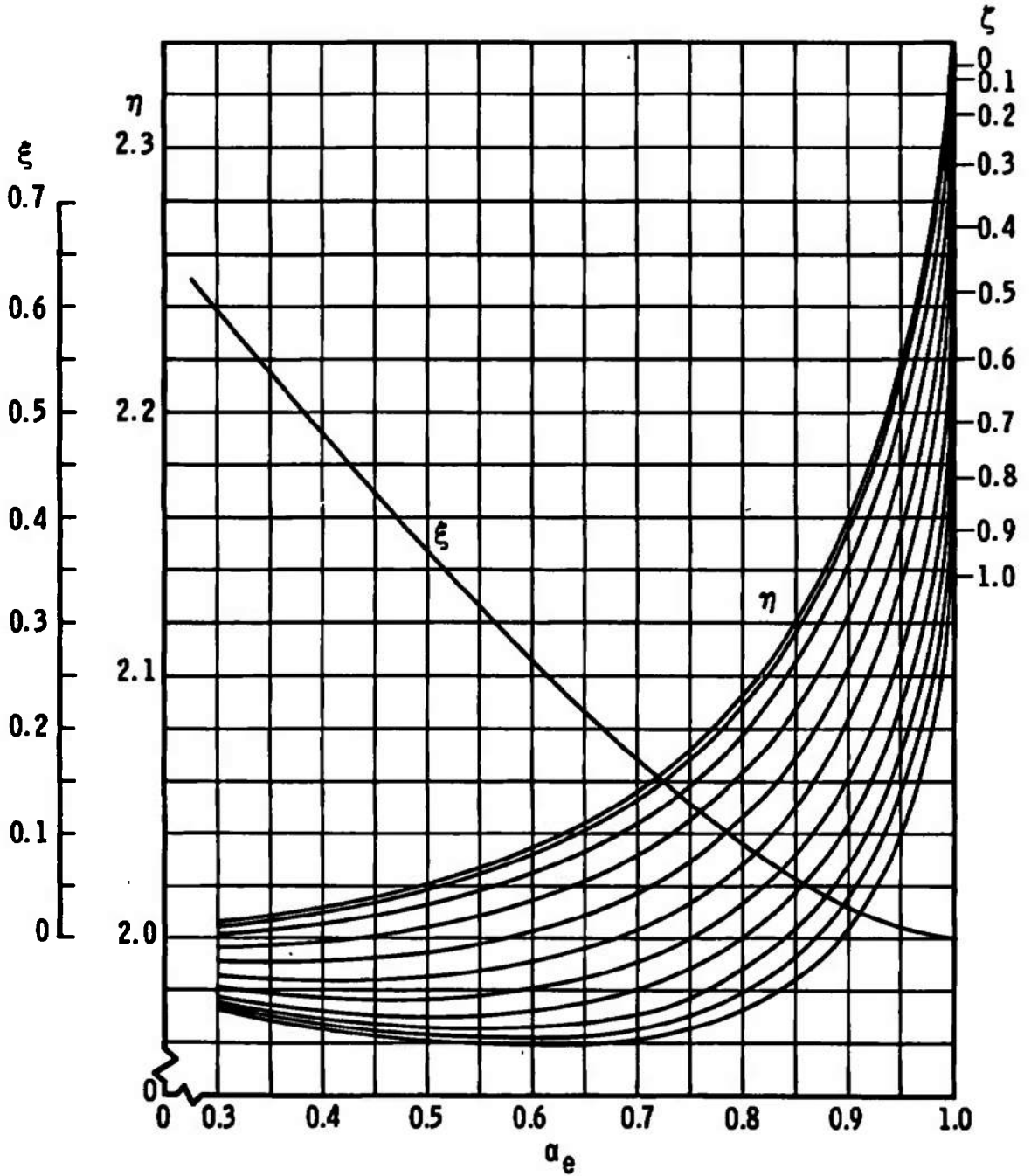


Figure B-2. Parameters in the Equation for  $T_r/T_w$ .

## NOMENCLATURE

$A^*$	Nozzle throat area
$C$	Chapman-Rubesin coefficient, $(\mu_w/\mu)(T/T_w)$
$C^*$	$C$ based upon $T^*$ , $(\mu_w/\mu^*)(T^*/T_w)$
$C_F$	Skin-friction coefficient, $\tau/q_\infty$
$C_p$	Pressure coefficient, $(p_w - p_\infty)/q_\infty$
$C_p'$	$C_p$ based upon reference conditions $(p_w - p_r)/q_r$
$h$	Enthalpy
$\vec{i}_b, \vec{j}_b, \vec{k}_b$	Unit vector in body coordinate system (see Fig. 4)
$K$	Nose drag coefficient (0.964 for spherically blunted cone)
$L$	Distance from apparent origin of source flow to center of rotation of model (see Fig. 4)
$L_r$	Distance from apparent origin of source flow to reference point (see Fig. 4)
$l_1$	Distance from model tip to center of rotation (see Fig. 4)
$M$	Mach number
$\dot{m}$	Mass flow rate
$\vec{n}$	Unit vector normal to local body
$Pr$	Prandtl number
$p$	Static pressure
$p_i$	Pressure indicated by means of a sensing orifice
$p_{inv}$	Inviscid cone static pressure
$p_o$	Tunnel reservoir pressure
$p_o'$	Free-stream pitot pressure
$p_w$	Wall static pressure obtained from $p_i$ by applying the orifice correction (see Appendix B)
$q$	Dynamic pressure $\rho_\infty U_\infty^2/2$
$\dot{q}$	Heat-transfer rate

$R_n$	Model nose radius
$Re_{\infty, x}$	Free-stream Reynolds number $U_{\infty} x \rho_{\infty} / \mu_{\infty}$
$Re_2$	Unit Reynolds number behind normal shock
$\bar{r}$	Radius vector from apparent origin of source flow to point on model surface
$r_b$	Local body radius (see Figs. 3 and 4)
$S$	Speed ratio
$St$	Stanton number, $q / \rho_{\infty} U_{\infty} (h_0 - h_w)$
$s$	Distance along model surface from stagnation point (see Fig. 3)
$T$	Temperature
$T^*$	Reference temperature
$T_0$	Stagnation temperature
$U_{\infty}$	Free-stream velocity
$\bar{v}$	Similarity parameter $M\sqrt{C/Re}$
$\bar{v}^*$	$M\sqrt{C^*/Re}$
$x$	Distance from nozzle exit to reference point
$x'$	Model coordinate parallel to axis (see Fig. 4)
$\alpha$	Model angle of attack (see Fig. 4)
$\alpha_e$	Energy accommodation coefficient
$\beta$	Angle between model surface normal and flow vector
$\gamma$	Ratio of specific heats
$\epsilon$	$(\gamma + 1) / (\gamma - 1)$
$\theta$	Local body angle
$\lambda$	Mean free path
$\mu$	Viscosity
$\rho$	Density
$\tau$	Skin friction
$\emptyset$	Roll angle (zero on windward side at positive angle of attack)



**SUBSCRIPTS**

2	Condition downstream of normal shock
inv	Inviscid cone condition
$l$	Local free-stream condition
o	Stagnation condition
r	Reference condition
w	Wall condition
$\infty$	Free-stream condition
=	Source flow condition converted to equivalent parallel flow at the reference condition